

FESOM2.1-REcoM3-MEDUSA2: an ocean-sea ice-biogeochemistry model coupled to a sediment model

Ying Ye¹, Guy Munhoven², Peter Köhler¹, Martin Butzin^{1,3}, Judith Hauck¹, Özgür Gürses¹, and Christoph Völker¹

¹Alfred-Wegener-Institut Helmholtz-Zentrum für Polar- und Meeresforschung (AWI), P.O. Box 12 01 61, 27515 Bremerhaven, Germany

²Laboratoire de Physique Atmosphérique et Planétaire, Université de Liège, B-4000 Liège, Belgium

³MARUM — Center for Marine Environmental Sciences, University of Bremen, Bremen, Germany

Correspondence: Ying Ye (Ying.Ye@awi.de)

Abstract.

This study describes the coupling of the process-based Model of Early Diagenesis in the Upper Sediment (MEDUSA version 2) to an existing ocean biogeochemistry model consisting of the Finite-volume Sea ice-Ocean Model (FESOM version 2.1) and the Regulated Ecosystem Model (REcoM version 3) ~~with flexible stoichiometry of organic matter. Atmospheric CO₂~~. Atmospheric CO₂ in the model is a prognostic variable which is determined by the carbonate chemistry in the surface ocean. The model setup and its application to a pre-industrial control climate state is described in detail. In the coupled model, ~~550 PgC~~ 1390 PgC are stored in the top 10 ~~cm~~ cm of the bioturbated sediment, mainly as calcite, but also to ~~12~~ 10% as organic matter. Simulated atmospheric CO₂ ~~reached 282 ppm stabilizes at ~ 295 ppm after 2000 years~~ years of the coupled simulation, ~~which is close to the initially assumed value of the pre-industrial CO₂ level~~ in line with the CO₂ level expected from the climate forcing conditions. Sediment burial of carbon, alkalinity and nutrients in the coupled simulation is set to be ~~partly~~ compensated by riverine input. The spatial distribution of biological production is altered depending on the location of riverine ~~nutrient input~~ , the changes in input and reduction of sedimentary input as well as the strength of local nutrient limitation, while the global productivity is not affected substantially. With this coupled ocean-sediment system the model is able to simulate the carbonate compensation feedback under moderate perturbation of CO₂ in the atmosphere.

15 1 Introduction

The ocean plays a key role in the global carbon cycle. It stores about 37,200 PgC (Keppeler et al., 2020), more than 40 times as much carbon as the atmosphere, which contained 884 PgC (or 417 ppm) in the year 2022 (Lan et al., 2023). About 25–30% of the global anthropogenic CO₂ emissions are taken up by the world oceans (Friedlingstein et al., 2022).

~~CO₂~~ CO₂ enters the ocean through gas-exchange, where it dissolves in seawater. A unique feature of dissolved CO₂ is that it reacts with water to form carbonic acid (~~H₂CO₃~~ H₂CO₃), which is instable and dissociates as a function of temperature, salinity and pressure into bicarbonate (~~HCO₃⁻~~ HCO₃⁻), carbonate (~~CO₃²⁻~~ CO₃²⁻) and hydrogen (~~H⁺~~ H⁺) ions (Zeebe and Wolf-Gladrow, 2001). The dissolved inorganic carbon (DIC), which is the sum of ~~CO₂, HCO₃⁻ and CO₃²⁻~~ CO₂, HCO₃⁻ and CO₃²⁻,

is distributed in the ocean via circulation. Part of the carbon in the surface ocean is also taken up via photosynthesis by marine phytoplankton and exported into the ocean interior via the sinking of dead organic matter. When stored in the deep ocean, this carbon reduces the surface concentration of DIC and allows for further CO_2 uptake from the atmosphere. Another important process in the marine carbon cycle is driven by calcifying plankton. These organisms produce calcium carbonate (CaCO_3) shells whereby CO_2 is released back into the atmosphere. These processes which all influence the surface-to-depth-gradient in DIC are also summarized as the so-called marine carbon pumps (Volk and Hoffert, 1985). Some of the particulate carbon (i.e., particulate organic carbon and CaCO_3 , ca. 1% of primary production; Sarmiento and Gruber, 2006) escapes dissolution and remineralization in the water column and sinks to the seafloor, where it might be buried. These particles are then removed from the relatively fast cycling of carbon at the surface of the Earth.

The storage of carbon, alkalinity and nutrients in sediments introduces an additional slow timescale to carbon cycling, and overall increases the carbon storage in the sediment-ocean system. The global burial flux of particulate organic carbon (POC) in marine sediments has been reported to be in a range of 160–2600 PgC kyr^{-1} (Burdige, 2007; Dunne et al., 2007; Sarmiento and Gruber, 2006; Muller-Karger et al., 2005). In total $\sim 280 \sim 280$ PgC kyr^{-1} are buried as CaCO_3 in marine sediments of which 100–150 PgC kyr^{-1} find their way into sediments of the deep-sea below at least 1 km of water depth (Sarmiento and Gruber, 2006; Dunne et al., 2012; Cartapanis et al., 2018; Hayes et al., 2021).

Furthermore, marine sediments play an important role as they provide records of the Earth's past climate. They react via the carbonate compensation feedback to any changes in the marine carbon cycle, in which the deep ocean carbonate ion concentration is brought back to its initial values after a perturbation on a multi-millennial timescale via sediment dissolution of CaCO_3 (Broecker and Peng, 1987).

Anthropogenic carbon emissions represent a rapid carbon cycle perturbation and in high-emission scenarios (Meinshausen et al., 2011), may ultimately lead to the massive dissolution of CaCO_3 in seafloor sediments over the next millennia (Archer et al., 1997). This carbonate compensation feedback contributes to a reduction of the long-term airborne fraction of anthropogenically emitted CO_2 from more than 20% if only the atmosphere-ocean is considered to be less than 10% (Archer et al., 2009; Köhler, 2020). This additional oceanic uptake of anthropogenic carbon through the dissolution of CaCO_3 , however, operates on a multi-millennial timescale, and is therefore only of interest for the geological fate of fossil emissions, but not for our near future. Hence, understanding processes controlling the sediment-ocean exchange and quantifying the carbon storage in marine sediments are crucial to explain transient behaviour over changing climates, e.g. the glacial-interglacial CO_2 variations (e.g. Brovkin et al., 2012; Köhler and Munhoven, 2020), and to predict the long-term ocean sequestration of anthropogenic carbon (Archer et al., 2009; Köhler, 2020).

All ocean biogeochemistry models incorporate a scheme to describe the fate of biogenic material that reaches the seafloor, but differ in their complexity (Munhoven, 2021, and references therein). The most simple schemes start from a reflective boundary condition, where all material reaching the seafloor is remineralized and returned to solution. More complex schemes consider a single, vertically integrated mixed-layer sediment box with a complete mass balances for the particles settling to the seafloor. Even higher complexity is found in vertically resolved sediment models describing diagenetic reactions, mechanical changes of dissolved and solid components as well as burial fluxes out of the surface sediment.

FESOM2.1-REcoM3, consisting of the Finite-volume Sea ice-Ocean Model 2.1 and the Regulated Ecosystem Model 3, is one of the ocean biogeochemistry models, which so far includes a simple one-layer sediment model (Gürses et al., 2023). REcoM3 describes the marine ecosystem at medium complexity with two phytoplankton classes including silicifiers and calcifiers, two zooplankton classes representing mixed zooplankton and polar macrozooplankton, and considers flexible stoichiometry of C , N , Si , Fe , $CaCO_3$, and chlorophyll. Various iron sources (sediment, dust and rivers) are implemented into REcoM3 and the model also has the option to simulate the cycles of ^{13}C and ^{14}C (^{13}C and ^{14}C) (Butzin et al., 2023). The sediment layer-box used so far in REcoM3 ensures the mass conservation by a complete remineralization of material sinking into the sediment-box. It represents processes in the surface sediment and is useful for short-term simulations, since the characteristic time scales of early diagenetic processes are often of the order of days to months, while long-term burial via sedimentation (which compensates riverine inputs from continental weathering) acts on time scales of thousands of years. Kriest and Oschlies (2013) have shown that the introduction of a sediment box makes models more robust against the uncertainties of the remineralization length scale, compared to models that remineralize everything in the water column. However, without considering sediment-ocean fluxes and feedbacks in more detail the model would not be able to reasonably simulate transient changes over glacial/interglacial timescales.

In Sect. 2), we describe the coupling of FESOM2.1-REcoM3p, a model configuration targeted for paleo-application, with MEDUSA2, the Model of Early Diagenesis in the Upper Sediment (Munhoven, 2021). MEDUSA2 is a process-based sediment module that offers a complex alternative to the previously used simple one-layer sediment. This is the first realisation of such an ocean-sediment setup of the marine carbon cycle with flexible stoichiometry of organic matter. In comparable existing alternatives (e.g. Kurahashi-Nakamura et al., 2020; Moreira Martinez et al., 2016) stoichiometry was kept fixed. This feature enables our model to simulate the growth limitation and community composition of phytoplankton in a more realistic way so that the biological carbon pump has a higher flexibility to react to climate change (Seifert et al., 2022; Schartau et al., 2007; Hohn, 2009). The final model configuration, referred to as FESOM2.1-REcoM3p-MEDUSA2, is applicable to relevant questions in paleoclimate research and should be able to provide new insights into the long-term dynamics of the marine carbon cycle. The coupled ocean-sediment simulation of this configuration under pre-industrial climate conditions is analysed in Sect. 3), along with transient simulations with perturbations in atmospheric CO_2 , while its applications to question of the last glacial cycle are envisaged in future, more targeted studies.

2 Methods

2.1 Model description

2.1.1 REcoM3p – A REcoM3 configuration for paleo research

REcoM is an ocean biogeochemistry and ecosystem model describing cycles of carbon, oxygen and nutrients (nitrogen, silicon and iron) with varying intracellular stoichiometry in phytoplankton, zooplankton and detritus. REcoM3 is the most recent release version and a detailed description of this version including its coupling to FESOM2.1 is given by Gürses et al. (2023).

90 The configuration REcoM3p used here has on the one hand reduced complexity with respect to functional groups of the modelled ecosystem and considered only one generic zooplankton and one detritus class, instead of two in the full version of REcoM3 (Fig. 1). As in the full version, diatoms and small phytoplankton which include calcifiers (only calcite producers, no aragonite) are considered here. The total 22 biogeochemical tracers cover nutrients (~~dissolved inorganic nitrogen (DIN),~~ ~~dissolved silicate (DSi) and dissolved iron (DIN, DSi and DFe)~~, two types of phytoplankton (diatoms and small phytoplankton) 95 with the state variables C, N and chlorophyll, as well as biogenic silica in diatoms and calcite in small phytoplankton, one zooplankton with C and N pools, one detritus with the state variables C, N, calcite and opal, dissolved organic matter with C and N pools, ~~dissolved inorganic carbon (DIC), alkalinity (Alk) and oxygen (DIC, Alk and oxygen)~~. The biological cycling of iron is described using a fixed Fe:N ratio in phytoplankton, zooplankton and detritus. The same parameter values were used as described in Gürses et al. (2023) and only two parameters were tuned for the reduced food web and coarser resolution (see 100 Tab. D1 ~~);~~ in the appendix).

So far REcoM3 only included a single-layer sediment. Particles sinking out of the bottom water boxes enter this sediment layer and go through remineralization (organic particles) and dissolution (calcite and opal) following a simple first-order decay approach: organic matter remineralization is neither dependent on O₂ availability nor does it follow different redox pathways; carbonate dissolution proceeds irrespective of the ambient saturation state (similarly to the dissolution in the water column). 105 The approach is thus equivalent to a classical reflective boundary with temporal buffering. The fluxes of solutes back to the bottom water boxes are derived from the remineralization and dissolution rates of the solids via the elemental ratios that characterize them. While the main aim of this study is the replacement of this simple sediment with the more complex sediment representation of the MEDUSA2 model, we keep this configuration as an alternative option for comparisons (labelled R_{sedbox} – see Sect. 2.4 below).

110 On the other hand, REcoM3p contains some extensions of relevance for the planned paleo applications when compared to the version described by Gürses et al. (2023): First, atmospheric CO₂ concentrations are calculated assuming that the atmosphere can be represented as a homogeneous carbon reservoir. The carbon cycle on land (continental biosphere) is not considered. Temporal changes in the atmospheric volume mixing ratio of CO₂ (X_{CO_2} , in ppm) then solely result from the globally integrated air-sea CO₂ flux, given by

$$115 \frac{\delta X_{CO_2}}{\delta t} \frac{\delta X_{CO_2}}{\delta t} = - \frac{\rho_{air}}{m_{atm}} \frac{\rho_{air}}{m_{textatm}} \cdot 10^6 \int F_{CO_2} dA,$$

where F_{CO_2} (mol m⁻² s⁻¹) is the regional air-sea CO₂ flux (calculated according to Wanninkhof (2014)), dA integrates over the ocean area, $\rho_{air} = 0.02897$ kg mol⁻¹ is the molar mass of dry air (from Picard et al. (2008), rounded here to four significant figures) and $m_{atm} = 5.1352 \cdot 10^{18}$ kg is the mass of the dry atmosphere (Trenberth and Smith, 2005). The factor 10⁶ serves to convert from mol fractions to ppm.

120 Second, a riverine source of DFe dissolved iron (DFe) was added to the already existing two sources from dust and marine sediments. Furthermore, due to the coupling to MEDUSA2, the sedimentary source of iron can be calculated in two ways: 1) in a fixed ratio to degradation of particulate organic nitrogen (PON) in the benthic layer as described in Gürses et al. (2023, Eq. A67 in Appendix A); 2) in a fixed ratio to the diffusive flux of DIN dissolved inorganic nitrogen (DIN) calculated

by MEDUSA2 in the coupled simulations. Elrod et al. (2004) demonstrated a clear correlation between the iron flux out of
125 sediments and the oxidation of organic matter on shelves, with a Fe : N ratio that is much higher than typical Fe : N ratios
in sinking organic matter. Under anoxic conditions in sediments, the flux of iron is increased due to the greater solubility of
ferrous iron. To represent this effect, we applied a higher Fe : N ratio (3 $\mu\text{mol Fe} : 20 \text{ mmol N}$) for the flux of iron from the
sediment to the water column than the ratio of 1 $\mu\text{mol Fe} : 30 \text{ mmol N}$ that we used for remineralization in the water column.
The same Fe : N ratio is used for both methods to calculate the sedimentary input of iron. A comparison of source strengths
130 for iron is discussed in Sect. 3.2.

Third, carbon isotopes were recently implemented into REcoM3p, as described in Butzin et al. (2023). However, the imple-
mentation of carbon isotopes into MEDUSA2 is not yet finished, which is why we here use REcoM3p with carbon isotopes
switched off.

When coupling REcoM3 to FESOM2.1 there remain some minor tracer conservation issues, that are related to the use
135 of an unstructured grid and need to be addressed. Although small (e.g., $0.53\% \text{kyr}^{-1}$ for the global Si inventory in the
ocean, i.e., $0.48 \text{ TmolSi yr}^{-1}$, which is smaller than the uncertainty on most input and output fluxes to and from the ocean
(Tréguer et al., 2021)), such imbalances may accumulate in an unfavourable way during simulation experiments run for tens
of thousands of years and longer. We therefore included a spatially uniform mass correction at the end of each coupling cycle
(every 50 model years – see below) so that the total inventory of Si is strictly conserved. A similar approach was adopted for
140 DIC, Alk, DIN and O_2 .

2.1.2 The sediment model MEDUSA2

MEDUSA is a time-dependent one-dimensional numerical model of coupled early diagenetic processes in sea-floor surface
sediments. The original model version (MEDUSA v1) was described in Munhoven (2007). MEDUSA v1 has evolved to
become MEDUSA2 which allows for a flexible chemical composition of the sediment, of the network of chemical transfor-
145 mations that describe the diagenetic processes (e.g. denitrification, etc.), and chemical equilibria to consider. It also offers a
variety of Application Programming Interfaces (APIs) for coupling it to ocean models with different grid configurations and
biogeochemical components (Munhoven, 2021). Here, we provide only a general description of the MEDUSA2 configuration
used in this study; for details, including the exact equations and parameter values adopted, please refer to the technical report
“MEDUSA Setup and Selected Configuration Options” in the Supplement.

150 In MEDUSA a sediment column is divided into three realms (the optional fourth one, a Diffusive Boundary Layer at the
sediment-water-interface was not considered here). The topmost part from the sediment surface is called REACLAY and
encompasses the reactive mixed-layer where solids sinking from the bottom layer of the ocean are collected. This is where
chemical reactions take place, solids are transported by bioturbation and advection resulting from the continuous deposition of
new material, and solutes by molecular diffusion. The second major realm is the located underneath, and is called CORELAY.
155 It is made of a stack of sediment layers, typically 1 cm thick each. Here, no reactions or mixing take place: solids are buried and
preserved in this realm which is building up a synthetic sediment core. REACLAY and CORELAY are connected by an thin
transitional layer (TRANLAY) which acts as a short-term (numerical) storage buffer and which can also be seen as the topmost

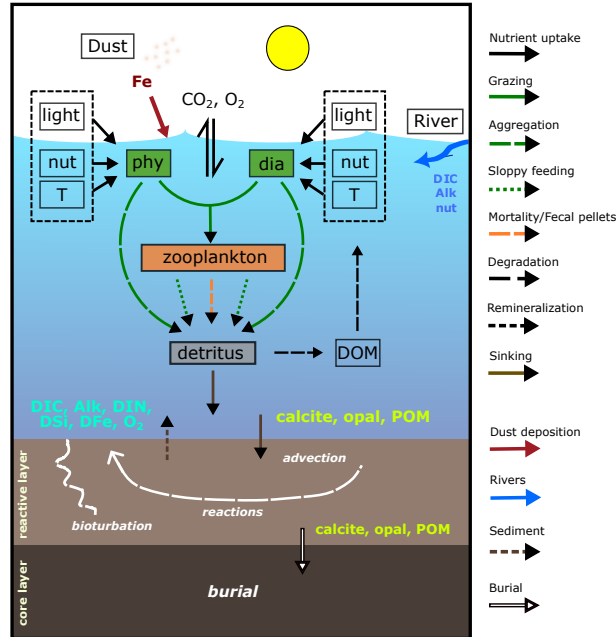


Figure 1. Schematic diagram of the components and interactions in REcoM3p coupled with the sediment model MEDUSA2 (modified and extended from Gürses et al. (2023, Fig. 2)). Small phytoplankton (**phy**) and diatoms (**dia**) take up inorganic nutrients (**nut**) and grow in dependence on **light** and temperature (T). One generic **zooplankton** consumes phytoplankton. Phytoplankton aggregation, zooplankton sloppy feeding, mortality and fecal pellets generate sinking **detritus**. Sinking detritus degrades to dissolved organic matter (**DOM**) which then remineralizes to dissolved inorganic carbon (DIC) and nitrogen (DIN). **Calcite**, **opal** and particulate organic matter (**POM**) reaching the seafloor enter the reactive layer of sediments, where accumulation, bioturbation, degradation and dissolution take place. Dissolved products of these processes (**DIC**, **Alk**, **DIN**, **DSi**, **DFe** and ΘO_2) go back to the bottom water by diffusion. The solids accumulate and are buried further in the core layer. Sources of DIC, Alk and nutrients to the ocean include sediments and rivers and dust deposition is an additional source of iron.

layer of CORELAY. In ~~our coupled configuration the~~ MEDUSA2 [configuration used here](#), sediment columns (one per seafloor grid element) ~~only resolve a 10~~ [resolve a 50](#) cm thick reactive surface sediment layer on a vertical grid with ~~21 points~~ [71 points](#) [to take into account diagenetic processes acting at depths greater than 10](#) cm, [such as organic degradation by sulfate reduction](#). The grid point spacing is not regular but increases with depth in the sediment ~~in order to allow~~ for a better representation of the strong subsurface solute concentration gradients. ~~The burial flux from the reactive layer into the core layer were monitored in our simulations, but not the changes of solids in the core layer~~ [Only the uppermost 10](#) cm [are mixed by bioturbation](#). There is no lateral exchange between sediment columns.

165 MEDUSA has already been coupled to several ocean biogeochemistry and Earth System Models (Moreira Martinez et al., 2016; Kurahashi-Nakamura et al., 2020; Munhoven, 2021). Coupling to ocean models is done through so-called ‘applications’ in the MEDUSA code. We introduced a new application `medusa-fesom-recom` which controls 1) the reading of

FESOM2.1-REcoM3p input and conversion into format and units that MEDUSA requires, 2) the selection of processes and global rate parameter values for tracing the evolution of the concentrations of solids and solutes considered, and 3) the writing of the resulting diffusive solute exchange with the ocean to a file for usage by FESOM2.1-REcoM3p and the obtained burial loss of solids into the sediment core. These burial losses can be used to monitor and/or regulate oceanic mass balances of carbon, alkalinity and the main nutrients (nitrogen and silicon).

Consistent with the input from FESOM2.1-REcoM3p, we chose a MEDUSA2 configuration with five solids (clay, calcite, opal and two types of organic matter) and ~~six~~ nine solute components (CO_2 , HCO_3^- , CO_3^{2-} , O_2 , NO_3^- ~~and~~ H_4SiO_4 , NH_4^+ , SO_4^{2-} ~~and~~ HS^-). The two types of organic matter are needed to account for the variable stoichiometry in REcoM3p. Processes altering the content of solids and solutes in sediments include calcite dissolution, ~~oxic respiration of organic matter, organic matter degradation by denitrification~~ organic degradation by aerobic respiration, denitrification and sulfate reduction, opal dissolution, and chemical equilibria of the carbonate system in the porewaters. Manganese and iron reduction are not considered for organic matter degradation since their contribution is negligible at the global scale (Thullner et al., 2009). REcoM3p only calculates formation and dissolution of calcite and does not represent aragonite. Correspondingly, only calcite dissolution in sediments is considered in the MEDUSA2 application `medusa-fesom-recom`.

As mentioned above, in the model setup organic matter can get degraded through ~~oxidation by either oxygen or via denitrification, aerobic respiration, nitrate and sulfate reduction~~, i.e., organic matter is preserved and buried once it reaches a sediment depth which is devoid of O_2 ~~and~~ NO_3^- ~~and~~ SO_4^{2-} . Bottom water concentrations of O_2 and NO_3^- are taken from FESOM2.1-REcoM3p output, while the SO_4^{2-} concentration is derived from the bottom water salinity following Dickson et al. (2007) since FESOM2.1-REcoM3p does not explicitly represent sulfur. NH_4^+ and HS^- concentrations at the sediment-water interface are set to 0 throughout the ocean (Thullner et al., 2009). This may result in too high preservation rates of organic matter in shallow shelf regions with high input rates of organic matter. Beyond nitrate, MEDUSA2 has previously been used with coupled Mn and Fe reduction and oxidation cycles (Munhoven, 2021). Sulfate reduction could also be easily added as a further oxidative pathway for organic matter. These additional degradation pathways are, however, not considered here, as including these processes requires a much finer vertical resolution and deeper reaching columns in the sediment model (e.g., 340 nodes instead of 21 in the JEASIM application in Munhoven, 2021).

Biological components in REcoM3p have variable intracellular stoichiometry and thus the seafloor deposition fluxes of POC and PON (particulate organic nitrogen) have no fixed ratio. However, in MEDUSA2 degradation of particulate organic matters (POM) is calculated for POM classes with a fixed stoichiometry each. We therefore defined two end-member classes of POM in MEDUSA2 in which $Q = C : N$ is fixed with $Q_1 = 106 : 21$ and $Q_2 = 200 : 11$, respectively, representing the minimum and maximum C:N ratio simulated in the seafloor deposition flux in REcoM3p. The total outgoing fluxes of PON from REcoM3p (F_N^o) were then partitioned into two incoming contributions F_N^{i1} and F_N^{i2} , according to

$$F_N^{i1} = \frac{Q_2 - Q}{Q_2 - Q_1} \cdot F_N^o \quad (1)$$

$$F_N^{i2} = \frac{Q - Q_1}{Q_2 - Q_1} \cdot F_N^o \quad (2)$$

where $Q = F_C^o/F_N^o$ is the ratio of the bulk POC flux (F_C^o) to the PON flux (F_N^o) that reaches the seafloor in REcoM3p. The carbon fluxes carried by the two POM classes are finally calculated by multiplying the nitrogen fluxes F_N^{i1} and F_N^{i2} with the respective C : N ratios:

$$F_C^{i1} = Q_1 \cdot F_N^{i1} \quad (3)$$

$$205 \quad F_C^{i2} = Q_2 \cdot F_N^{i2} \quad (4)$$

The degradation time scale of organic matter depends on its elemental composition (i.e. the C : N ratio) (Amon and Benner, 1994; Martin et al., 1987). In the water column in FESOM2.1-REcoM3p, we considered a faster remineralization of nitrogen compared to carbon with the ratio of 1.1:1 (ρ_{DetN} and ρ_{DetC} in Gürses et al. (2023), Tab. A8). The rate law expression chosen for the oxic degradation of organic matter in the sediment is more complex: it is linear in the concentration of organic matter in porewaters (with separate expressions for [POM₁] and [POM₂]), and includes a Monod-type (hyperbolic) limitation with respect to the concentration of oxygen in the porewaters ([O₂]—see Tab. ?? for details). ~~Based on tuning experiments for a better representation of the sediment POC content, we adopted a 10-fold~~, supplementary material Sect. 3.2). Organic matter degradation through nitrate and sulfate reduction is described in a similar way but taking into account the inhibition by oxygen (supplementary material Sect. 3.3 and 3.4); organic matter oxidation by sulfate reduction is inhibited by oxygen and nitrate. ~~We adopted a 100-fold~~ faster degradation rate for the low-C:N organic matter class (k_{ox1} / k_{ox2} for POM₁) than for the high-C:N organic matter class (k_{ox2} / k_{ox1} for POM₂) (Soetaert et al., 1996).

Besides organic matter, calcite and opal, the simulated sediment contains an inert component, which we refer to as ‘clay’ here for the sake of simplicity, and which is ultimately of continental origin. It stems from dust particles deposited over the sea surface and from terrestrial materials transported to the oceans by rivers. In our model setup, annual mean dust deposition from Albani et al. (2014) is considered as the oceanic clay input into sediments. ~~Further, a globally constant input of $2.5 \cdot 10^{-8} \text{ mol illite cm}^{-2} \text{ year}^{-1}$ over the seafloor (10-fold higher than Heinze et al. (1999) based on tuning experiments) was added, assuming that clay has the composition of illite. This uniform flux is meant to represent the terrestrial component in clay which is redistributed by ocean internal processes, such as mixing and resuspension. The strength of this flux is a result of tuning experiments and the total clay input~~ This dust deposition distribution leads, however, to unrealistically low sedimentation (solid deposition) rates at seafloor depths shallower than 3000 m, typically by a factor of 20–50, but occasionally by more than 100, when compared to the empirical relationship of Middelburg et al. (1997). We therefore increased the deposition rate of lithogenic material (‘clay’) by $10^{-2.4-Z/1250} \times 0.1 \times 2650 \text{ kg m}^{-2} \text{ yr}^{-1}$, where Z is the depth below sea-level (in m), 0.1 is the volume fraction of solids close to the sediment surface (for a porosity of 0.9), and 2650 is the density of lithogenic material (in kg m^{-3}). This way, the global distribution of seafloor sedimentation rates is in better agreement with the the empirical relationship of Middelburg et al. (1997). The resulting global distribution of clay input used in this study is shown in Fig. B1.

2.2 Coupling REcoM3p and MEDUSA2

FESOM2.1-REcoM3p and MEDUSA2 are sequentially coupled through file exchange. Sinking fluxes of POC, PON, opal (SiO₂) and calcite out of the bottom water boxes are saved as output files by FESOM2.1-REcoM3p and read as input files by

MEDUSA2 (Fig. 1). Furthermore, MEDUSA2 requires information on temperature, salinity and concentrations of alkalinity (Alk), DIC, oxygen, and nutrients in the bottom-most ocean model box. Temperature and salinity enter thermodynamic calculations in the sediment model and the bottom water concentrations are used in the calculation of diffusive fluxes between sediment and water column.

FESOM2.1-REcoM3p reads diffusive fluxes of nutrients including dissolved inorganic nitrogen (DIN) and dissolved silicate (DSi or H_4SiO_4), DIC, Alk and oxygen from the MEDUSA2 output file (Fig. 1). DFe input from sediments is derived from the diffusive flux of DIN, using a fixed Fe:N ratio. Other quantities that are calculated by MEDUSA2 are the permanent burial of carbon, organic matter, opal and calcite in the sediment core. This output is used to monitor ~~-, and partly compensate, and~~ compensate changes in the total mass balances of carbon and the other tracers in the ocean and reactive sediment. ~~For silicon and nitrogen we assumed that riverine input compensates the burial flux, while for Alk, a global riverine input was taken from Börker et al. (2020) representing weathering fluxes. Based on the sediment burial of carbon (POC and calcite, Table 2), we~~ tuned DIC river input to reproduce the pre-industrial level. The total riverine input ~~The burial loss is balanced by adding the same quantities as riverine input which~~ is distributed over the surface ocean in the model by scaling it with the local river runoff from the forcing data.

2.3 Model setup

2.3.1 Model configuration

FESOM2.1 employs unstructured meshes with variable horizontal resolution. The default mesh of FESOM2.1-REcoM3 (~~COREH~~ COREII mesh) has about 127 000 surface nodes with a nominal average resolution of ~~1 degree~~ degree and enhanced resolution in the equatorial belt and ~~in~~ at high latitudes going up to 25 km (Gürses et al., 2023). For testing the coupling with MEDUSA2 a reduced model resolution (PI mesh) is used here, containing 3140 surface nodes, corresponding to a median horizontal resolution of ~~260 km~~ km (Butzin et al., 2023). This configuration reduces computational costs and simplifies simulations over the time scale of thousands of years in order to approach deep ocean equilibrium and significant changes in marine sediments. MEDUSA2 is coupled to the bottom layers of the ocean model, ~~therefore~~. Therefore the horizontal grid within MEDUSA2 is always the same as in the ocean model.

Vertically, the ocean is divided into 47 layers and the layer thickness ranges from 5 m in the surface to 250 m in the deep ocean. The full free-surface formulation (zstar) was used, allowing vertical movement of all layers, to ensure tracer conservation in FESOM (Scholz et al., 2019, 2022). In this study, the model was retuned for the coarser resolution by reducing the maximum thickness diffusivity of the ~~Gent-McWilliams~~ Gent-McWilliams parameterisation from $3000 \text{ m}^2 \text{ s}^{-1}$ (used in the default FESOM2.1) to $1000 \text{ m}^2 \text{ s}^{-1}$.

2.3.2 Forcing and initial conditions

FESOM2.1 is initialised with ~~seasonal-winter~~ January temperatures and salinities from the Polar Science Center Hydrographic
265 Climatology (PHC3, updated from Steele et al. (2001)) and driven by annually repeated atmospheric fields using the Corrected
Normal Year Forcing Version 2.0 (CORE-NYF.v2, Large and Yeager, 2009).

The initial value of X_{CO_2} is 284.3 ppm following Meinshausen et al. (2017). Alk and DIC are initialised from version 2 of
the Global Ocean Data Analysis Project (GLODAPv2) data set (Lauvset et al., 2016), DIN and DSi from the Levitus World
Ocean Atlas climatology of 2013 (Garcia et al., 2014) and oxygen from the Levitus World Ocean Atlas climatology of 2018
270 (Garcia et al., 2019). The initial DFe field is based upon output from the Pelagic Interaction Scheme for Carbon and Ecosystem
Studies (PISCES) model (Aumont et al., 2015), as outlined in ~~(Gürses et al., 2023)~~ Gürses et al. (2023).

Dust input of iron at the sea surface is calculated based on monthly averages of dust deposition by Albani et al. (2014)
with a weight percentage for iron of 3.5% and a solubility of 2%. The riverine DFe input is based upon de Baar and de Jong
(2001), who estimate that the rivers transport 26 Gmol Fe as DFe to the oceans each year. These authors assume that about
275 90% of this is lost by flocculation when river water gets mixed with seawater, which reduces the actual input to the ocean to
2.6 Gmol Fe yr⁻¹. However, depending on types of catchment areas and the concomitant input of organic material which may
act as metal chelator, the river input of DFe can be significantly higher (Guieu et al., 1996; Krachler et al., 2005). We therefore
tuned our model by varying the river input of DFe (assuming an upper limit of 26 Gmol Fe yr⁻¹) to get a reasonable distribution
of DFe and of the simulated biological productivity, and finally adopted a total riverine DFe input of 5.2 Gmol Fe yr⁻¹. The
280 river ~~input~~ input of DFe is distributed at the sea surface by scaling with the river runoff, which is part of the CORE-NYF.v2
forcing.

2.4 Coupled ~~simulation~~ simulations with FESOM2.1-REcoM3p-MEDUSA2

A coupled simulation starts with a spinup run with FESOM2.1-REcoM3p ~~run~~ (R_{spinup}), followed by the pre-charging of
MEDUSA2 (Fig. 2). Subsequently, FESOM2.1-REcoM3p and MEDUSA2 are run alternately with a defined coupling fre-
285 quency of ~~50years~~ years (R_{coupled}).

2.4.1 FESOM2.1-REcoM3p spinup run (R_{spinup})

FESOM2.1 (without biogeochemistry) was run for 1000 years as a spinup of the ocean circulation. After that, REcoM3p
was switched on and run for another 1500 years to get a quasi-equilibrium of deep ocean concentrations. During these 1500
years, the exchange between ocean and sediment was calculated with the ~~alternative~~ original one-layer sediment representation.
290 Model output of the last 50 years was analysed as the initial conditions for R_{coupled} in Section 3.1.

2.4.2 Pre-charging of MEDUSA2

Continuous exchange of material between ocean and sediments alters both ocean chemical boundary conditions and the content
of the reactive sediment layer. The latter changes much ~~slower~~ more slowly due to low sedimentation rates. To reduce the com-

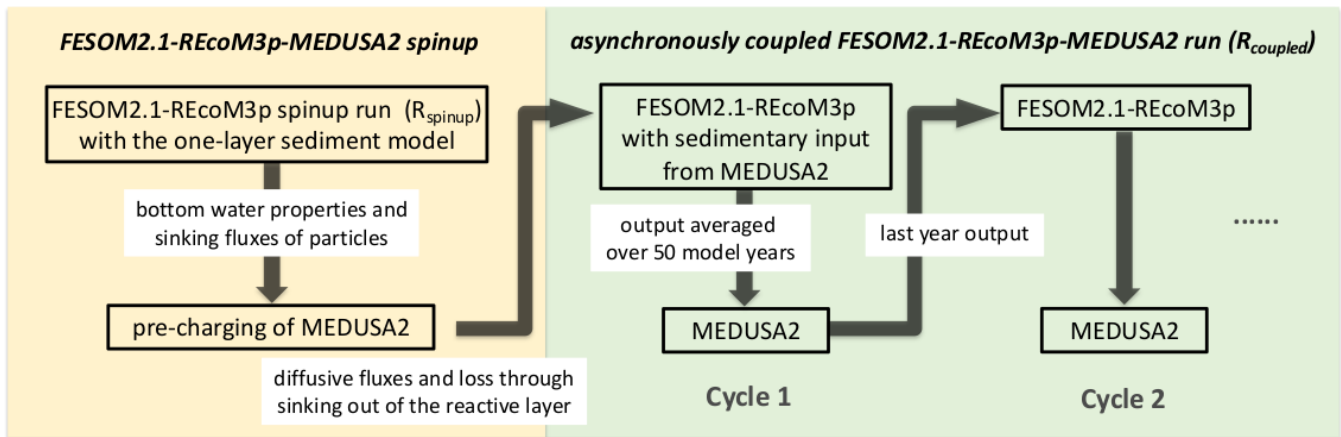


Figure 2. Workflow of a coupled FESOM2.1-REcoM3p-MEDUSA2 simulation.

putting time for getting significant changes in sediments, MEDUSA2 was first run for 100,000 years forced by the results from
 295 R_{spinup} so that the sediment layers in MEDUSA are charged before an interactive coupled FESOM2.1-REcoM3p-MEDUSA2
 simulation starts. This way, we may reach an initial seafloor sediment distribution that is as consistent as possible with the
 productivity pattern, the cycling in the water column and the boundary conditions prevailing at the seafloor (oxygenation,
 saturation state, etc).

2.4.3 Coupled simulation (R_{coupled})

300 Two simulations were started from the state of year 1500 in R_{spinup} and compared to demonstrate how carbon storage in sedi-
 ments affects the marine carbon cycle and atmospheric CO_2 - CO_2 (Fig. 2): (1) R_{sedbox} is the continuation of R_{spinup} from
 year 1500 to year 3500; (2) a coupled simulation R_{coupled} was conducted for 2000 model years starting with the precharged
 MEDUSA2 sediment layers (see previous section). A coupling frequency of 50 years was consistently applied between
 FESOM2.1-REcoM3p and MEDUSA2. For each coupling cycle, output of FESOM2.1-REcoM3p was averaged over 50 years
 305 before using it as input in MEDUSA2. The sediment-to-ocean fluxes (input to FESOM2.1-REcoM3p) were updated every
 50 years with results from the MEDUSA2 simulation. Within one coupling cycle the ocean-sediment exchange fluxes to be
 applied at each time step were kept constant. The outputs of R_{sedbox} and R_{coupled} were averaged over the last 50 years before
 comparison (Sect. 3.2).

~~Asynchronous coupling can affect mass conservation in coupled models since the exchange between models is temporally
 310 shifted. Here, we quantified this effect in a test simulation. The temporal change of the Si inventory was taken as a measure
 for mass conservation, since the balance of the silicon cycle is complete in our coupled simulations. The only Si flux out of the
 ocean-sediment system is the sediment burial of opal and the only input is the riverine flux of DSi into~~

2.4.4 Transient simulations with perturbations in atmospheric CO_2 (R_{pert1k} and R_{pert2k})

~~To demonstrate that the ocean-only setup of FESOM2.1-REcoM3p which is for mass conservation prescribed by burial flux. Thus, variations in the silicon inventory with time can only be explained by temporal offsets of REcoM3p-MEDUSA2 can be used to study transient climate changes, two experiments were conducted starting from the final state of R_{coupled} , adding 1000 and 2000 PgC into the atmosphere, respectively. With those experiments, the interactions between the atmosphere, ocean and sediment processes. An increase of total silicon by about 0.4 was observed in the test simulation. Based on this result, a spatially uniform mass correction was applied to bottom water concentrations in the coupled simulation at the end of each coupling cycle (in our study every 50 model years) so that the total inventory of Si is forced back to that at the beginning of the coupled simulations. The mass correction factor was calculated from the difference between the current inventory and that at the beginning of the coupled simulation. For DIC, Alk, DIN and O under idealised ocean acidification scenarios were examined. Both coupled experiments (R_{pert1k} and R_{pert2k}) were run for 2000 years and the temporal change in the atmospheric CO_2 , corrections were applied with the same correction factor concentration and calcite content in sediments was analysed.~~

2.4.5 Performance of the coupled model

FESOM coupled with REcoM spends about 80% of the total run time of a simulation on the tracer transport computations (Himstedt, 2023). An acceleration method was implemented for a parallel calculation of tracer advection and with two parallel tracer groups on 72 cores, a speedup by a factor of 1.8 was achieved for simulations with the reduced resolution using the PI mesh (Himstedt, 2023). In this study, each coupled FESOM2.1-REcoM3p-MEDUSA2 cycle (50 model years) is then completed within seven hours computation time on 72 cores, of which the MEDUSA2 related calculations require less than five minutes (i.e., of the order of 1% only).

3 Results and Discussion

3.1 FESOM2.1-REcoM3p spinup simulation with the one-layer sediment (R_{spinup})

Generally, the global and basin-averaged profiles of DIC, Alk, DIN, DSi and O_2 in the FESOM2.1-REcoM3p spinup run (R_{spinup}) agree well with GLODAPv2 (Large and Yeager, 2009) and WOA data (Garcia et al., 2019) (Fig. A1), particularly in ocean basins covering large areas of the open ocean. The modelled O_2 concentration in the Arctic Ocean is clearly lower than observed. This will be discussed in Sect. 3.2.5 below.

~~Averaged vertical profiles of DIC, Alk, DIN and DSi in ocean basins () in R_{spinup} , compared with GLODAPv2 (Large and Yeager, 2009) and WOA data (Garcia et al., 2019) which were used as initial conditions in simulations in this study.~~

The global net primary production (NPP) of 35 PgC yr^{-1} is lower than the satellite-based estimates but comparable to other modelling studies (see Gürses et al., 2023, Table 3 and references therein), e.g. $24.5\text{--}57.3 \text{ PgC yr}^{-1}$ in CMIP6 (Séférian et al., 2020). The larger part of NPP comes from the small phytoplankton (23 PgC yr^{-1}); diatoms contribute the remaining 12 PgC yr^{-1} . Carbon export out of the upper 100 m into the deep ocean is 6.6 PgC yr^{-1} . The slightly higher productivity and export found here compared to an NPP of 32.5 PgC yr^{-1} in the base version of FESOM2.1-REcoM3 (Gürses et al., 2023)

Table 1. Seafloor deposition and burial fluxes of POC (PgC kyr^{-1}), calcite (PgC kyr^{-1}) and opal (Pmol Si kyr^{-1}) in simulations and observation-based estimates, reported for the global ocean and ocean regions deeper than 1 km. R_{high} is shown here to demonstrate the impact of model resolution on the simulated seafloor deposition and this study rather focuses on the low-resolution simulations.

	Seafloor deposition					
	POC		calcite		opal	
	<u>global</u>	<u>> 1 km</u>	<u>global</u>	<u>> 1 km</u>	<u>global</u>	<u>> 1 km</u>
<u>R_{sedbox}</u>	<u>650</u>	<u>410</u>	<u>380</u>	<u>370</u>	<u>70</u>	<u>65</u>
<u>R_{coupled}</u>	<u>420</u>	<u>270</u>	<u>370</u>	<u>360</u>	<u>80</u>	<u>70</u>
<u>R_{high}</u>	<u>1380</u>	<u>415</u>	<u>300</u>	<u>260</u>	<u>90</u>	<u>70</u>
<u>Observed</u>	<u>930–5739^a</u>	<u>310–1029^b</u>			<u>22–40^c</u>	<u>79–84^d</u>

	Burial					
	POC		calcite		opal	
	<u>global</u>	<u>> 1 km</u>	<u>global</u>	<u>> 1 km</u>	<u>global</u>	<u>> 1 km</u>
<u>R_{coupled}</u>	<u>86</u>	<u>28</u>	<u>100</u>	<u>90</u>	<u>18</u>	<u>13</u>
<u>Observed</u>	<u>160–2600^e</u>	<u>2–300^f</u>	<u>280^g</u>	<u>100–150^h</u>	<u>7.1ⁱ</u>	<u>5.9–9.2^j</u>

Reference keys: B: Burdige (2007), C16: Cartapanis et al. (2016), C18: Cartapanis et al. (2018), D07: Dunne et al. (2007), D12: Dunne et al. (2012), Ha: Hayes et al. (2021), Hi: Hilton and West (2020), J: Jahnke (1996), M: Muller-Karger et al. (2005), N: Nelson et al. (1995), Sa: Sarmiento et al. (2002), Se: Seiter et al. (2005), T95: Tréguer et al. (1995), T13: Tréguer and De La Rocha (2013), T21: Tréguer et al. (2021).

^a B, D07, M, Sa; ^b B, J, M, Sa, Se; ^c D07, N, T95; ^d J, T21; ^e B, C18, D07, M; ^f B, C16, C18, D07, Hi, Ha, J, M, Se; ^g C18; ^h C18, D12, Ha, Sa; ⁱ T95; ^j Ha, T13, T95, T21

345 can be explained by the differences between the model setups: 1) a much coarser spatial resolution of the PI mesh used here and a different forcing data set, which result in differences in resolved physical processes (e.g., circulation and mixing) and thus in the environmental conditions for phytoplankton growth (e.g., light, temperature and nutrient supply); 2) REcoM3p uses a configuration with a single zooplankton class whereas the simulations in Gürses et al. (2023) contained two zooplankton classes; 3) additional iron input from rivers relieves iron limitation of phytoplankton growth in some regions.

350 Deposition fluxes from the ocean bottom layer onto the top of the sediments from different simulations and burial fluxes of POC, calcite and opal from the coupled simulation are summarized in Table 1 along with observation-based estimates. The simulated global deposition rate of POC (650 PgC kyr^{-1}) in R_{sedbox} is lower than the range of observation-based estimates ($930\text{--}5739 \text{ PgC kyr}^{-1}$) reported by Burdige (2007). This is not surprising since the global primary and export production in our model are both lower than observations. The simulated POC deposition rates (Fig. 3a) are in the same order of magnitude as
355 Dunne et al. (2007) but mainly occur on top of deep-sea sediments (deeper than 1 km). The contribution of the deposition rates in shallower waters (37%) underestimates the relative share of 67–82% obtained by others (Muller-Karger et al., 2005;

Burdige, 2007). Models with a coarse resolution do not resolve physical processes and thus the biological recycling of carbon in shelf regions well, likely leading to an unrealistic estimation of POC sinking into and accumulation in sediments. ~~This can be clearly seen in a comparison (Tab. 1) with a simulation at higher spatial resolution (R_{high}).~~ To quantify the effect of model resolution, we did a simulation with exactly the same model code and setup but at a higher resolution with 126,858 surface nodes ~~(R_{high}), i.e.,~~ as in Gürses et al. (2023)). The total POC deposition rate of ~~850~~1380 PgC kyr⁻¹ ~~comes closer to in R_{high} fits in~~ the estimated range, and the flux in shallower waters represents a larger fraction (8070%) of the global flux which falls within the range of estimates (67–82%). Here, we still consider model results with a coarse resolution which is commonly used for technical tests, allowing us to run a reasonable number of tuning experiments and coupled simulations over several
 365 thousands of years within a realistic time frame.

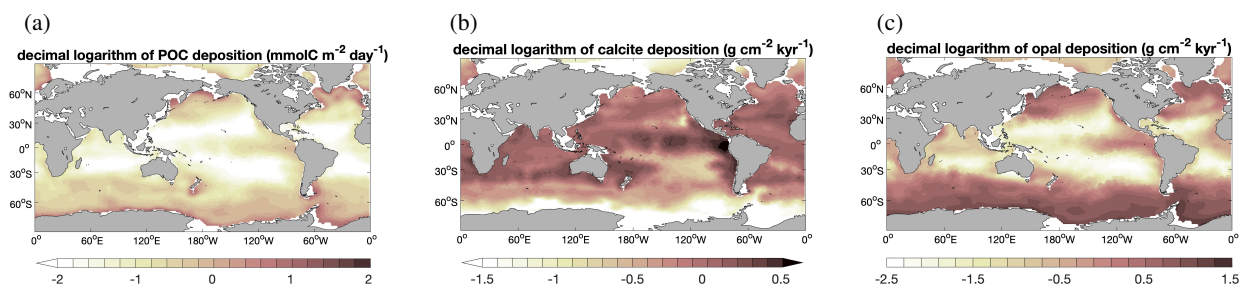


Figure 3. ~~Seafloor~~ Decimal logarithm of seafloor deposition rates of (a) POC ($\text{mmol C m}^{-2} \text{ day}^{-1}$, i.e., the same units as in Dunne et al. (2007)), (b) calcite ($\text{g cm}^{-2} \text{ kyr}^{-1}$) and (c) opal ($\text{g cm}^{-2} \text{ kyr}^{-1}$) ~~at seafloor~~ in $R_{\text{sedboxspinup}}$.

A total calcite deposition rate of 380 PgC kyr⁻¹ is found to reach the ocean-sediment interface in $R_{\text{sedboxspinup}}$, from which 370 PgC kyr⁻¹ happened in the deep ocean below 1-km water depth. Be aware that the omissions of aragonite and of the benthic production of CaCO_3 (e.g., by coral reefs) are important shortcomings of our approach. Buitenhuis et al. (2019) simulated three pelagic calcifiers and estimated a contribution of aragonite producers to shallow water export of CaCO_3 at
 370 100 m of at least 33%. Furthermore, coccolithophore and calcifying zooplankton together are reported to contribute to the global carbonate fluxes by 40–60% and the rest of the fluxes remains unexplained (Knecht et al., 2023), which also results in high uncertainty in the simulating calcifying organisms and CaCO_3 fluxes. Our model roughly reproduces the spatial pattern of the Th-normalized deposition fluxes (Hayes et al., 2021) with high fluxes in the North Atlantic and Arabian Sea (up to 2 $\text{g cm}^{-2} \text{ kyr}^{-1}$), lower fluxes in ~~the main part of the large areas in the~~ Pacific and Southern Ocean ($< 1 \text{ g cm}^{-2} \text{ kyr}^{-1}$,
 375 Fig. 3b). Only some parts of the eastern equatorial Pacific region, the modelled calcite fluxes are about two times higher than in Hayes et al. (2021) which might be caused by the too high calcite production in this region in the model.

The seafloor deposition rate of opal in $R_{\text{sedboxspinup}}$ is 70 Pmol Si kyr⁻¹, of which 65 ~~accounted for by those parts of the oceans that are more~~ Pmol Si kyr⁻¹ ~~take place at seafloor depths greater than 1 km deep~~ km. Observation-based estimates ~~show conflicting results available in the literature unfortunately provide a conflicting picture,~~ with 22–40 Pmol Si kyr⁻¹ for
 380 the total flux (Dunne et al., 2007; Nelson et al., 1995; Tréguer et al., 1995), while in the ocean that is deeper than 1 km 84 ± 17 Pmol Si kyr⁻¹ (Tréguer and De La Rocha, 2013; Tréguer et al., 2021) should settle. ~~Under the assumption that the~~

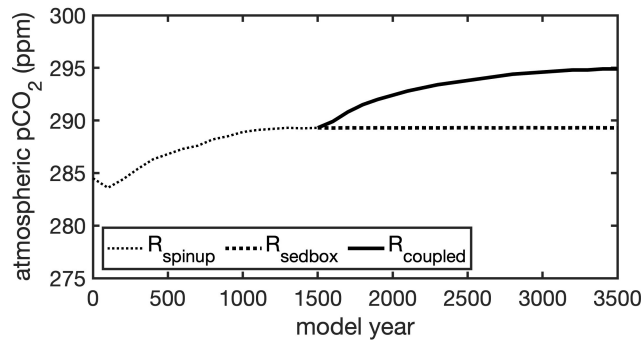


Figure 4. Simulated atmospheric CO_2 - CO_2 during 3500 model years: a FESOM2-REcoM3p spinup simulation with an integrated one-layer sediment (R_{spinup}) was run for 1500 years; after 1500 years the model with an integrated one-layer sediment was run for further 2000 years (R_{sedbox}) and a simulation coupled with MEDUSA2 (R_{coupled}) was branched off and run for 2000 years.

~~newer~~ Assuming that the more recent data are of better quality ~~we can~~, we conclude that the simulated opal deposition rates in the deep ocean agree well with reconstructions while for the total rates a revised data set seems necessary. The spatial distribution of opal fluxes agree qualitatively well with Hayes et al. (2021) with high fluxes at high latitudes in both hemispheres and moderate ones ~~along in~~ the eastern equatorial Pacific (Fig. 3c). However, the model shows much higher values in the Southern Ocean ~~which indicates~~, indicating that the Fe limitation of ~~diatoms over~~ diatom growth in the Southern ocean ~~in the model is somewhat too weak~~ is too weak in the model.

~~Seafloor deposition and burial fluxes of POC (PgC kyr^{-1}), calcite (PgC kyr^{-1}) and opal (Pmol Si kyr^{-1}) in simulations and observation-based estimates, reported for the global ocean and ocean regions deeper than 1 km. global > 1 km global > 1 km global > 1 km R_{sedbox} 650 410 380 370 70 65 R_{coupled} 580 390 380 370 80 70 R_{high} 850 160 440 370 45 35 Observed 930–5739^a 310–1029^b 22–40^c 79–84^d global > 1 km global > 1 km global > 1 km R_{coupled} 110 50 115 86 82 9.5 Observed 160–2600^e 2–300^f 280^g 100–150^h 7.1ⁱ 5.9–9.2^j~~

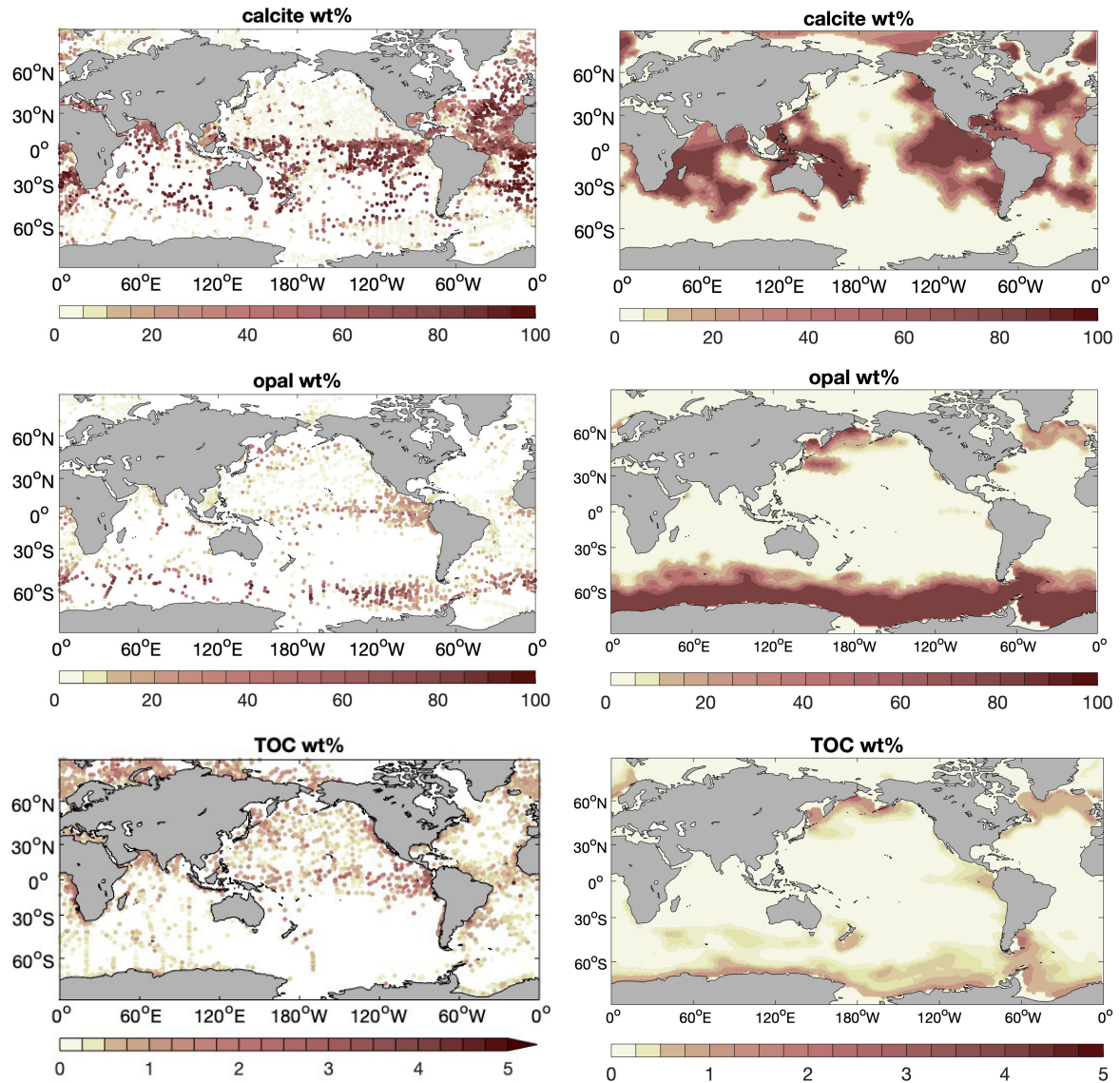
During the total 1500 simulated years the atmospheric CO_2 - CO_2 concentration first rises with time and reaches 289 ppm at the end of R_{spinup} (Fig. 4).

3.2 The coupled simulation with FESOM2.1-REcoM3p-MEDUSA2 (R_{coupled})

3.2.1 Sediment content

The weight percentage of sediment composition (Fig. 5) is compared in the following with the data compilation of the surface sediment composition of Hayes et al. (2021), ~~but note that the latter agrees widely~~. ~~It should be noted that this latter broadly agrees~~ with the alternative and ~~much~~ older compilation of Seiter et al. (2004).

400 Simulated calcite content in R_{coupled} (Fig. 5, ~~row 1 top row~~) exhibits high values (up to >9080%) in the Atlantic, tropical and subtropical South Pacific as well as the Indian Ocean, and lower values (near zero) in the North Pacific and ~~the~~ Southern



[Hayes et al. \(2021\)](#)

[R_{coupled}](#)

Figure 5. [Distribution \(weight %\) of \(top row\) calcite, \(middle row\) opal and \(bottom row\) total particulate organic carbon \(TOC\) in the sediment, averaged over the upper 10 cm of sediments. Left: data compilation of averages over the Holocene age and measurements reported for the surface sediment by Hayes et al. \(2021\); Right: results from simulation R_{coupled}.](#)

Ocean. Also, the calcite-rich sediments along the Atlantic mid-ocean ridge are reproduced to some extent in the model. This simulated pattern generally agrees well with Hayes et al. (2021).

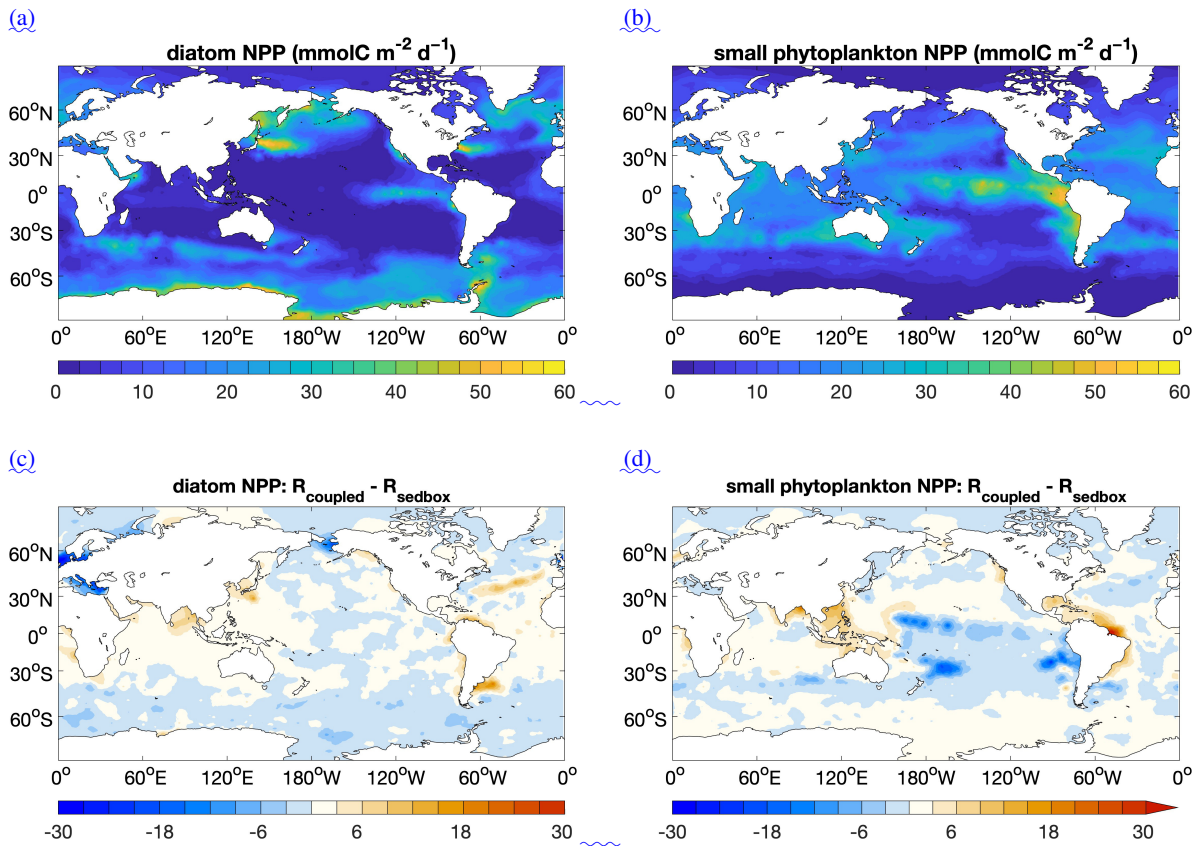


Figure 6. NPP ($mmolC\ m^{-2}\ day^{-1}$) of (a) diatoms, and (b) small phytoplankton in R_{sedbox} and the difference in NPP (c, d) between the two simulations ($R_{coupled}$ -minus- R_{sedbox}).

Opal content (Fig. 5, [row 2 middle row](#)) is elevated at high latitudes in the North Pacific and North Atlantic Ocean, as well as in the Southern Ocean at the Antarctic Polar Front. This is also seen in the data compilation. The opal distribution mainly reflects the diatom productivity (Fig. 6a) and opal deposition rates (Fig. 3). The latter has a similar pattern as ^{230}Th -normalized ^{230}Th -normalized estimates by Hayes et al. (2021), whereas much higher fluxes are found in the model over large areas in the Southern Ocean. This could lead to a likely overestimation of opal content in sediments, although not many observations are available for these areas. The opal belt in the equatorial eastern Pacific is smaller and less pronounced in the model than observed. This is related to the somewhat too strong iron limitation of diatoms in this region in our model.

Simulated sediment POC

[Simulated sediment TOC](#) (Fig. 5, [row 3](#)) shows a strong contrast between shallow-water regions and open oceans which is not seen in the data compilation. In large areas of the open ocean and low-latitude shallow-water regions, the simulated POC content is negligibly low compared with data, whereas in most of the high-latitude shallow-water regions, it is up to one order of magnitude higher than the measurements. In the [bottom row](#)) is elevated at high latitudes in the Atlantic Ocean, North Pacific

and Southern Ocean, similar to opal. Also significantly higher TOC preservation is found in the eastern equatorial Pacific and the Indian sector of the Southern Ocean the simulated POC has the same order of magnitude as the data compilation. A. Beside the contribution by diatoms, small phytoplankton in the model also has a high productivity in this region (Fig. 6b). Only a small amount of TOC is present in sediments in large areas of the open ocean. The global pattern of sediment TOC content roughly agrees with data compilation, although a detailed comparison of POC content in the southern hemisphere, particularly in the South Pacific Ocean, is not possible due to lack of data. Yet in the comparison to Hayes et al. (2021) we found that the simulated deposition rates along the Antarctic coasts are about one order of magnitude higher than the reconstruction, which likely contributes to overestimate the POC fraction in the sediments. Another reason for a too high POC fraction in shallow water sediments could be the missing of riverine input of lithogenic material. Rivers deliver several petagrams of suspended sediments to the ocean each year (Peucker-Ehrenbrink, 2009; Milliman and Meade, 1983). Most of these particles are deposited close to the continental margins. Such localized effects are not considered here but might need to be investigated in future studies. The magnitude of TOC preservation in shallow waters and upwelling regions is somewhat lower compared to data compilation. This may in part be explained by the fact that the modelled biological production and thus the deposition flux to sediments are both lower than observation-based estimates (Sect. 3.1).

420
425
430 ~~1em 1em 1em Hayes et al. (2021)~~ R_{coupled} Distribution (weight %) of (row 1) calcite, (row 2) opal and (row 3) total particulate organic carbon (TOC) in the sediment. Left: data compilation by Hayes et al. (2021); Right: results from simulation R_{coupled} .

3.2.2 Degradation of organic matter in sediments

~~Two Three~~ different pathways of degradation of organic matter in sediments are considered here: ~~oxic degradation and denitrification~~ aerobic respiration, nitrate reduction and sulfate reduction. This setup offers the possibility to have a closer look at their roles in different ocean regions. Figure 7 (left) shows the fraction of oxic degradation in the total degradation. In large areas of ~~shows~~ the deep-sea sediments, oxic degradation dominates (up to 100%), whereas denitrification mainly takes place in shallow water sediments, which results in very low concentrations of in pore waters at high latitudes and in some logarithm of organic carbon degradation rate ($\mu\text{molC cm}^{-2} \text{yr}^{-1}$) by aerobic respiration (a), nitrate reduction (b) and sulfate reduction (c), integrated over the upper sediment layers of 10 cm. Aerobic respiration and denitrification roughly follow the pattern of POC deposition flux (Fig. 3a), while sulfate reduction mainly concentrates in much smaller areas at high latitudes and some upwelling regions with high biological productivity and thus large input of organic matter. concentrations in these regions are far below its half-saturation concentration (Fig. 7 right), potentially leading to an overestimation of the preservation of organic matter in our simulation since no further oxidative degradation is considered in our setup when is exhausted.

445 The globally integrated denitrification rate of 23 is within the range of previous estimates of 12–168 (DeVries et al., 2013; Thullner et al., albeit at the lower end and much lower than the range of 230–285 of Middelburg et al. (1996). In large areas of the deep-sea sediments, aerobic respiration is the dominant degradation process. Nitrate reduction has lower rates than aerobic respiration in most regions of the world ocean, except for the high-latitude North Pacific where porewater oxygen is fully consumed through

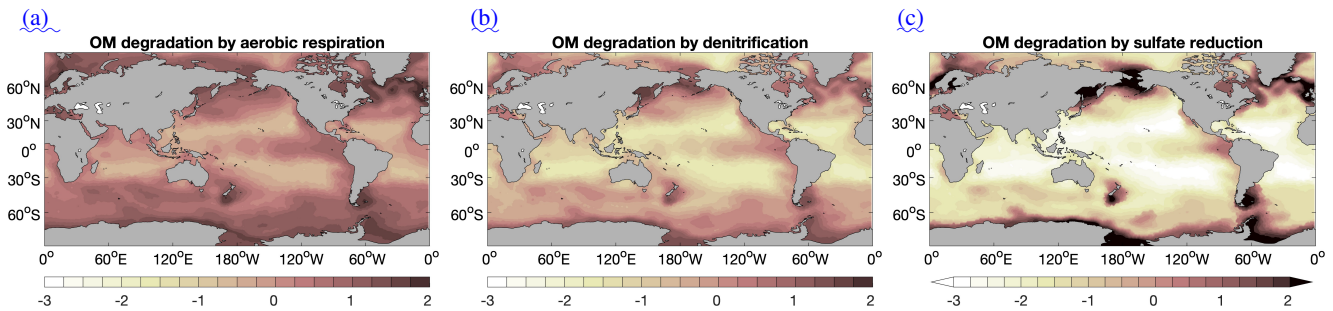


Figure 7. Fraction (%)–Decimal logarithm of vertically integrated organic matter carbon degradation by in total degradation rates (left $\mu\text{molC cm}^{-2} \text{yr}^{-1}$) and the ratio of by aerobic respiration ($R^{\text{NO}_3^-}$) concentration in pore water at the bottom of the bioturbated sedimentary mixed layer, denitrification (10 below the sediment-water interface) to its half saturation concentration (5–parameters C_{nmr1} and C_{nmr2} in Table ?? sulfate reduction (c). The dotted line in rates are vertically integrated over the right-hand panel indicates where top 10 cm of the concentration is equal to its half saturation concentration modelled reactive sediment layer, i.e., the mixed layer.

organic matter degradation. In high-latitude regions, high rates of sulfate reduction reach up to two orders of magnitude of those of the other two processes.

About 39 Globally in the modelled 50 cm reactive sediment layer, about 33 TmolC yr^{-1} are degraded is remineralized, where 45% is contributed by aerobic respiration in $R_{\text{comp}}^{\text{total}}$, which falls in, 9% by nitrate and 46% by sulfate reduction. Our total carbon remineralisation is comparable to Sarmiento and Gruber (2006) ($\sim 27 \text{ TmolC yr}^{-1}$), while previously reported data-based estimates and model results cover a large range from 19 to 260 TmolC yr^{-1} (Thullner et al., 2009; Burdige, 2007; Smith and Hollibaugh, 1990).

Aerobic respiration of 15 TmolC yr^{-1} falls below the range of estimates based on oxygen consumption (33–97 TmolC yr^{-1}) for deep-sea sediments (Jahnke, 1996; Christensen, 2000; Andersson et al., 2004; Seiter et al., 2005; Glud, 2008; Jørgensen et al., 2022) but ($> 1000 \text{ m}$) (Jahnke, 1996; Christensen, 2000; Andersson et al., 2004; Seiter et al., 2005; Glud, 2008; Jørgensen et al., 2022) and is much lower than estimates of oxygen consumption for the global sediments (99–212 TmolC yr^{-1} , see Snelgrove et al., 2018; Stratmann et al., 2019; Jørgensen et al., 2022) but substantially higher than some model results (e.g. 3.1 TmolC yr^{-1} by Thullner et al. (2009)).

Denitrification removes about 2.9 TmolN yr^{-1} is within the range of previous estimates of 1–12 TmolN yr^{-1} (DeVries et al., 2013; Thullner et al., 2009) but lower than the range of 16–20 TmolN yr^{-1} of Middelburg et al. (1996).

Sulfate reduction accounts for 46% of the global carbon mineralisation rate in our model, within the range between 30–76% reported in previous studies (Canfield et al., 2005; Jørgensen and Kasten, 2006; Thullner et al., 2009). The highest values of sulfate reduction are around 400 $\mu\text{molC cm}^{-2} \text{yr}^{-1}$, in line with the data compilation by Middelburg et al. (1997) for sediments in shallower waters.

3.2.3 Solute exchange across the sediment-water interface

The diffusive flux of DIC from the sediment to the ocean shows a similar pattern to DIN, with high fluxes in regions with high input of organic matter into sediments (Fig. 8a and c). One exception for DIN is the net flux of DIN from the ocean into the sediment ~~along the coasts in the North Pacific~~ in regions along the Pacific coasts. In Fig. 7 these regions are characterised by ~~a high fraction of denitrification in the total degradation~~ high rates of denitrification, which results in a substantial reduction of DIN in the ~~pore water~~ porewater and thus a net diffusion of DIN from the ocean bottom water to the sediment.

Diffusive fluxes of O_2 show more or less the opposite pattern to DIC. In regions where the seafloor deposition rate of organic matter is high (Fig. 8d), e.g., in the Northern Hemisphere around 60° or in the Southern Ocean, degradation of organic matter leads to a high O_2 flux from the ocean to the sediments as well as high DIC flux from the sediment to the ocean. ~~In the large areas at lower latitudes on the other hand, the DIC and flux distributions are uncoupled. Here, it is rather the Alk flux (Fig. 8b) that the DIC flux is correlated to.~~

The Alk flux distribution (Fig. 8b) looks more complex and is the result of two processes that have opposite effects: degradation of organic matter decreases the alkalinity in ~~pore water~~ porewater, while calcite dissolution increases it. Therefore, in those regions where the organic matter degradation rate in the surface sediment is high (i.e., where O_2 uptake is high – Fig. 8d) alkalinity in ~~pore waters~~ porewaters may get lowered to the extent that there is a net influx of alkalinity from the ocean bottom water to the sediment. In the Atlantic, the Indian Ocean and parts of the Pacific Ocean where calcite inputs to the sediment are high, alkalinity in ~~pore water~~ porewater is clearly increased and there is a net diffusive flux of alkalinity out of the sediment, into the ocean bottom water. ~~The effect of calcite dissolution is also reflected in the DIC diffusive flux at low to mid-latitudes which is, however, less pronounced in Fig. 8a than in Fig. 8b due to different color scales.~~

3.2.4 Burial fluxes out of the reactive layer

The simulated POC burial flux in the global sediment (~~41086~~ 1086 PgC kyr^{-1}) is lower than the observed range (160–2600 PgC kyr^{-1} , Tab. 1), consistent with the comparison for the productivity and sinking fluxes. In the deep-sea sediments the simulated flux (~~5028~~ 28 PgC kyr^{-1}) is within but close to the lower end of the observed range (2–300 PgC kyr^{-1}), reflecting again the inability of our model to represent shallow-water processes with the current resolution.

Similarly, the simulated global burial flux of CaCO_3 (~~86100~~ 6100 PgC kyr^{-1}) is much lower than the observation-based estimate (280 PgC kyr^{-1}), while the deep-sea burial of ~~8295~~ 295 PgC kyr^{-1} is close to the lower end of the observed range of 100–150 PgC kyr^{-1} . The observation-based estimates suggest a roughly equal distribution between shallow and deep-sea environments, while the model simulates only about 5% of the global calcite burial in sediments at depths shallower than 1 km. The possible causes ~~are~~ is the omission of some CaCO_3 producers in REcoM3p ~~and the coarse resolution which have~~ which has been already discussed in Sect. 3.1.

The simulated opal burial in deep-sea sediments (~~9.513~~ 513 Pmol Si kyr^{-1}) ~~slightly~~ exceeds the observed range (5.9–9.2 Pmol Si kyr^{-1}), ~~while the~~ reflecting an overestimation of opal deposition in large areas in the Southern Ocean. It is difficult to compare the modelled global burial of ~~4218~~ 218 Pmol Si kyr^{-1} ~~is clearly higher than with~~ the only available but relatively old estimate of

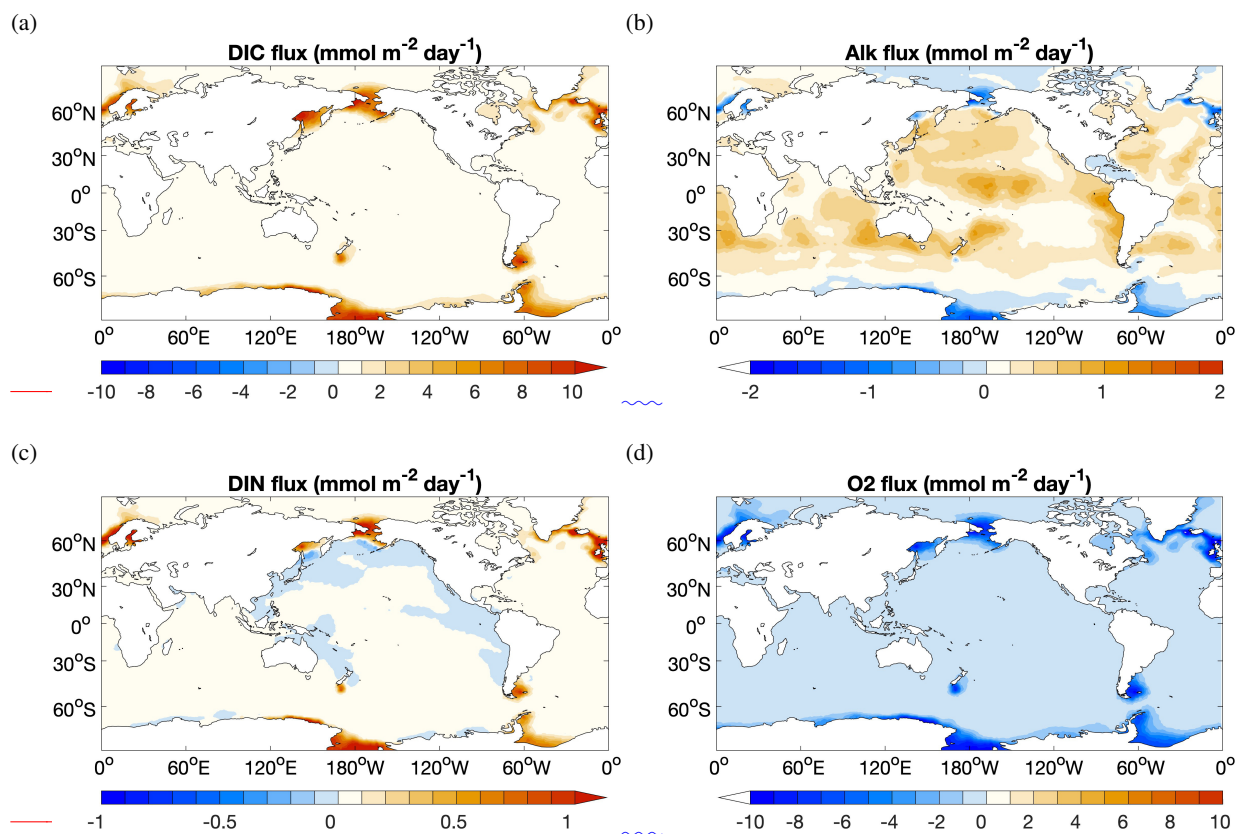


Figure 8. Diffusive flux of DIC, Alk, DIN and O₂ from the sediment to the ocean ($\text{mmol m}^{-2} \text{day}^{-1}$). Sources for the ocean are shown as positive values.

7.1 Pmol Si kyr^{-1} by Tréguer et al. (1995). ~~This study also reported the lowest value of the~~ which is even lower than other estimates for the deep-sea burial. This issue has been already mentioned by discussing opal deposition flux in Sect. 3.1.

3.2.5 Impact of the complex sediment on productivity and nutrient supply

The globally averaged vertical distributions of DIC, Alk, O₂ and nutrients do not differ much between R_{sedbox} (Fig. A1) and R_{coupled} (Fig. 9). The O₂ distribution in the Arctic Ocean is largely considerably improved in R_{coupled} . In MEDUSA2 ~~consumption by degradation~~, the oxic degradation rate of organic matter is calculated in dependence of depends on the O₂ concentration in ~~sediments, while using the sediment, whereas in~~ the one-layer sediment model, O₂ consumption in sediments is calculated with a fixed O₂:C ratio and subtracted from the bottom water O₂ concentration, likely leading to an overestimation of degradation of organic matter and the lowering of O₂ concentrations in the bottom water. This also applies to other regions with high deposition of organic matter such as the Southern Ocean and parts of the ~~Atlantic-Pacific~~ Ocean which also show small improvements in the O₂ profiles.

The marine NPP in the coupled simulation R_{coupled} is nearly the same as in R_{sedbox} : ~~it only slightly increases from 35 to 36.~~
The spatial distribution of ~~the~~ NPP differences between the ~~coupled simulation and R_{sedbox}~~ two simulations (Fig. 6) reveals higher productivity by both diatoms and small phytoplankton in coastal regions with large riverine nutrient inputs (DIN and
515 DSi, Fig. 10c and d), which were not considered for R_{sedbox} .

~~(a) 7.7em (b) — (c) 7.7em (d) — NPP () of (a) diatoms, and (b) small phytoplankton in R_{sedbox} and the difference in NPP (c, d) between the two simulations (R_{coupled} minus R_{sedbox}).~~

Nutrient supply in the simulations using MEDUSA2 or the one-layer sediment differs in two ways. First, the total diagenetic flux of nutrients from the sediment to the ocean is lower when using MEDUSA2 (Fig. 10a and b; Table 2), since particles
520 sinking into sediment can be stored there: a part is degraded ~~and or~~ dissolved in the reactive layer and ~~comes back to bottom water by diffusion~~ the remineralization products released to the porewaters from where they may diffuse back to the overlying ocean bottom waters, while the rest is buried in the deeper ~~sediments (Munhoven, 2021)~~ core layers (Munhoven, 2021). This storage and burial delay nutrient recycling and reduce the sedimentary nutrient source when compared to the full degradation and dissolution which takes places in the single-layer sediment. Second, the current riverine source of nutrients considered in
525 the coupled simulation is estimated from the solid burial flux that leaves the reactive sediment layer to be transferred to the core layer in MEDUSA2. This additional source brings nutrients directly into surface waters near river mouths (Fig. 10c and d). As a result, diatom productivity shows a clear decrease in the North Sea and the Bering Sea (Fig. 6c) where DIN, DSi and DFe from sediments are all significantly reduced (Fig. 10a and b) and no riverine input can cover the loss (Fig. 10c and d).

In R_{coupled} , ~~42.4~~ 416.8 Tmol Si yr⁻¹ are delivered by rivers, while the sedimentary source only decreases from 73.2 Tmol Si yr⁻¹
530 in R_{sedbox} to ~~65.9~~ 62.9 Tmol Si yr⁻¹ (Table 2). On the other hand, the riverine input of ~~4.2~~ 20.1 Tmol N yr⁻¹ cannot compensate the decline in the sediment input from 8.1 to ~~6.0~~ 5.0 Tmol N yr⁻¹. The nutrients supplied by rivers are, however, directly available for phytoplankton living in surface waters and can still induce phytoplankton growth in areas adjacent to river mouths (Fig. 6c and d), particularly in regions where sedimentary input does not change much (e.g. tropical and subtropical regions). The sedimentary source of iron strongly decreases as well (Table 2), however, the intensity of iron limitation for phytoplankton
535 does not change significantly, since the riverine source is much higher and covers most of the regions where sedimentary input becomes smaller in R_{coupled} .

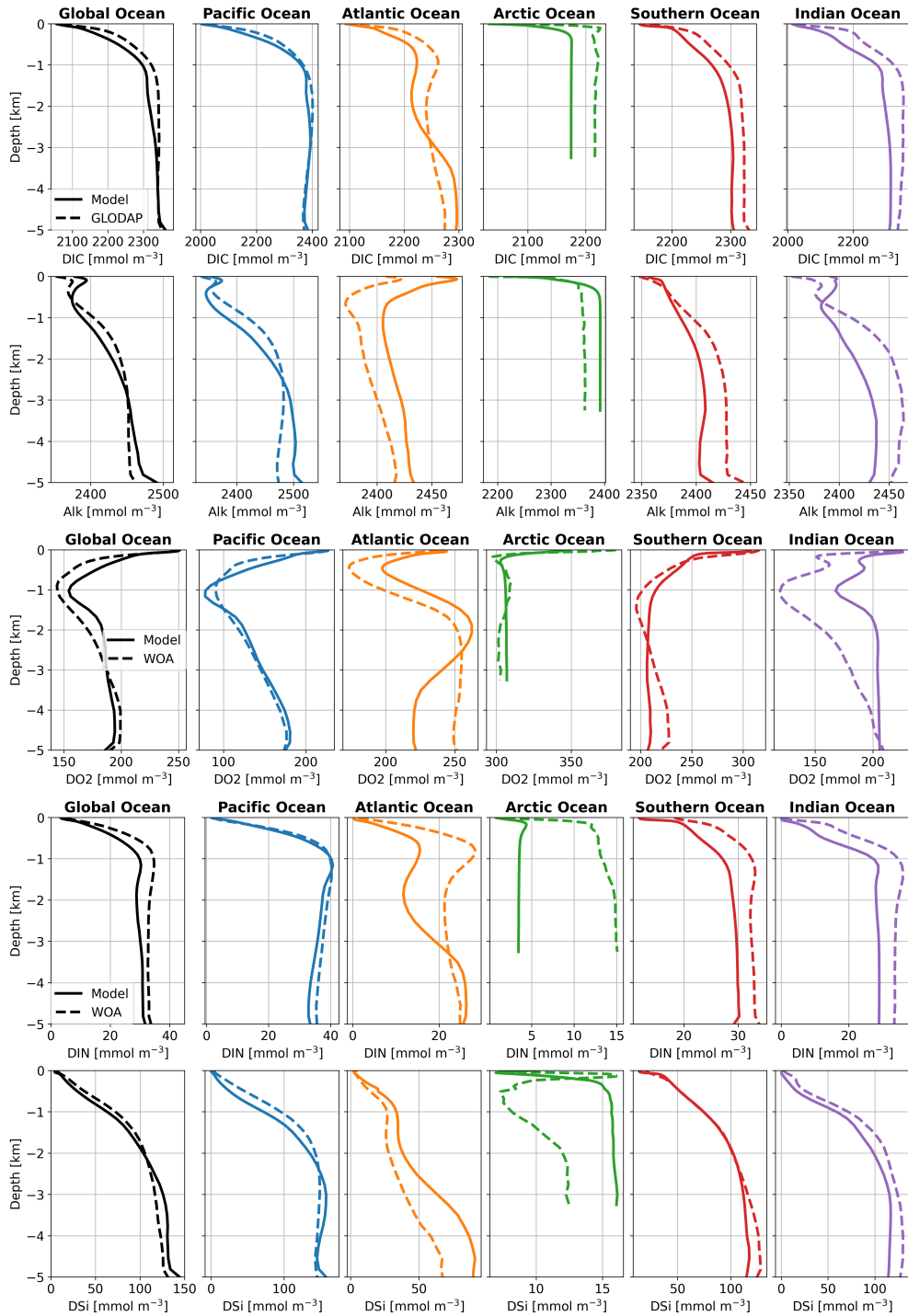


Figure 9. Averaged vertical profiles of DIC, Alk, O_2 , DIN and DSi in ocean basins (mmol m^{-3}) in R_{coupled} , compared with GLODAP and WOA data which were used as initial conditions in simulations in this study.

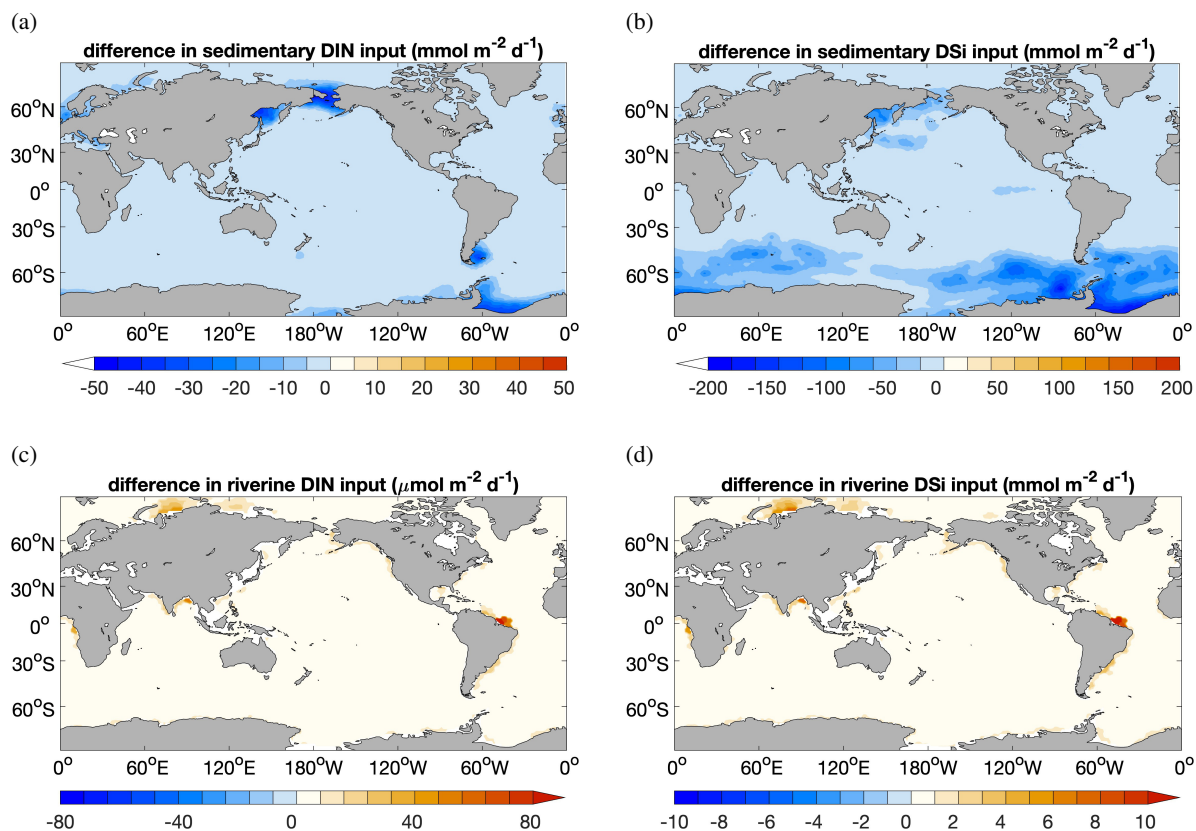


Figure 10. Decrease of sedimentary input of (a) DIN ($\text{mmol m}^{-2} \text{d}^{-1}$) and (b) DSi ($\text{mmol m}^{-2} \text{d}^{-1}$) in R_{coupled} compared to R_{sedbox} ; additional riverine input of (c) DIN ($\mu\text{mol m}^{-2} \text{d}^{-1}$) and (d) DSi ($\text{mmol m}^{-2} \text{d}^{-1}$) in coupled simulations R_{coupled} ($\text{mmol m}^{-2} \text{day}^{-1}$ $\text{mmol m}^{-2} \text{d}^{-1}$). Change in sedimentary input of DFe has an identical spatial pattern as DIN since the iron source is calculated based on DIN source with a constant Fe:N ratio.

Table 2. Fluxes averaged over the last 50 years of the simulations. ~~Positive fluxes are into~~ Diffusive flux of iron from sediments to the ocean ~~or into sediments~~ is derived from the diffusive flux of DIN, using a fixed Fe:N ratio. ~~Continued on next page.~~ Note that Burial flux is calculated for the units here are ~~bottom of the reactive sediment layer at 50 cm.~~

Positive fluxes are into the ocean or into sediments. ~~Continued on next page.~~ Note that the units here are Tmol yr⁻¹, ~~not,~~ not Pg yr⁻¹.

	Ocean balance	R _{sedbox}	R _{coupled}
C	riverine input	0	+9.1 <u>9.0</u>
	diffusive flux out of sediment	+85.8	+64.5 <u>52.9</u>
	seafloor deposition (POC)	-54.2	-48.4 <u>35.5</u>
	seafloor deposition (Calc)	-31.5	-31.6 <u>30.9</u>
	air-sea gas exchange	-0.2	+1.5 <u>0.3</u>
(Tmol year ⁻¹)	Sediment balance		
	seafloor deposition (POC)	+54.2	+48.4 <u>35.5</u>
	seafloor deposition (Calc)	+31.5	+31.6 <u>30.9</u>
	diffusive flux out of sediment	-85.8	-64.5 <u>52.9</u>
	burial (POC)	0	-8.9 <u>1.9</u>
	burial (Calc)	0	-7.1
Alk	Ocean balance		
	riverine input	0	+11.0 <u>14.0</u>
	diffusive flux out of sediment	+47.9	+45.0 <u>41.8</u>
	seafloor deposition (PON)	+9.0	+8.0 <u>5.6</u>
	seafloor deposition (Calc)	-62.9	-63.3 <u>61.8</u>
(Tmol year ⁻¹)	Sediment balance		
	seafloor deposition (PON)	-9.0	-8.0 <u>5.6</u>
	seafloor deposition (Calc)	+62.9	+63.3 <u>61.8</u>
	diffusive flux out of sediment	-47.9	-45.0 <u>41.8</u>
	burial (POM)	0	+1.2 <u>0.1</u>
	burial (Calc)	0	-14.3 <u>14.1</u>

Table 2. ... continued

	Ocean balance	R_{sedbox}	R_{coupled}
N	riverine input	0	+1.2-0.1
	diffusive NO_3 flux out of sediment	+8.1	+6.0-5.0
	seafloor deposition	-8.0	-7.1-5.2
	Sediment balance		
(Tmol year ⁻¹)	seafloor deposition	+8.0	+7.1-5.2
	diffusive NO_3 flux out of sediment	-8.1	-6.0-5.0
	burial (PON)	0	-1.2-0.1
	Ocean balance		
Si	riverine input	0	+12.1-16.8
	diffusive flux out of sediment	+73.2	+65.9-62.9
	seafloor deposition	-72.4	-77.7-80.4
	Sediment balance		
(Tmol year ⁻¹)	seafloor deposition	+72.4	+77.7-80.4
	diffusive flux out of sediment	-73.2	-65.9-62.9
	burial (opal)	0	-12.1-16.8
Fe (Gmol year ⁻¹)	dust	+5.8	+5.8
	rivers	+5.2	+5.2
	diffusive flux out of sediment	+1.2	+0.7-0.3

3.2.6 Impact of the complex sediment representation on atmospheric CO₂ and carbon storage

The oceanic carbon pools evolved towards equilibrium concentrations during R_{coupled} by adjusting the gas exchange and the fluxes between ocean and sediment. The atmospheric CO₂ in R_{coupled} ~~declined to 282~~ increased to 295 ppm after 2000 years which is ~~just slightly below~~ higher than the pre-industrial value of 284.3 ppm used ~~initially in R_{spinup} to initialize the model,~~ but consistent with the climate state determined by the CORE-NYF.v2 forcing. The air-sea gas exchange is not completely balanced at the end of the run with a net positive CO₂ flux from the atmosphere to the ocean of ~~1.50~~ 3 TmolC yr⁻¹ (Table 2), indicating that the ~~atmosphere-ocean-sediment~~ atmosphere-ocean-sediment system has not yet reached its equilibrium. This can be seen in the temporal development of CO₂ (Fig. 4) and change in fluxes into and out of the sediment over time (Fig. C1).

We quantified the size of the carbon storage in the reactive sediment layer at the end of R_{coupled}, being aware of that the system is still in a transient state. Compared to R_{sedbox}, the ocean contains about ~~90 Pg more DIC and about 550~~ 150 Pg less DIC. About 1390 PgC is accumulated in the sediment surface layer in R_{coupled}, mainly as calcite but with a ~~12~~ 10% contribution from POC (Table 3). Emerson and Hedges (1988) estimated a POC storage of 150 PgC in the mixed layer of sediments and Parameswaran et al. (2024) recently reported that their modelled upper 10 cm of oceanic sediments harbors approximately ~~171~~ 171 Pg TOC, while Archer (1996) reported that 800 ~~PgC~~ PgC is stored as calcium carbonate within the 10 cm thick bioturbated layer. Our simulated carbon storage in the surface sediment (~~70~~ 130 PgC as POC and ~~480~~ 1060 PgC as calcite) is ~~lower than these observation-based estimates. One major cause is the underestimation of shallow-water sediments in the coarse-resolution simulation.~~ comparable with these observation- and model-based estimates. In R_{sedbox}, POC and calcite are almost completely degraded and dissolved in the single-layer sediment and thus the reservoir sizes of carbon in the sediment are close to zero.

The ~~lowering~~ slow increase of atmospheric CO₂ is mainly explained by the long-term storage of material in the sediments combined with the riverine input of carbon and alkalinity, which subsequently determines how DIC is distributed into its three species CO₂, HCO₃⁻, and CO₃²⁻, from which only CO₂ can exchange with the atmosphere (Zeebe and Wolf-Gladrow, 2001).

Table 3. Carbon stocks (PgC) in the ~~ocean-sediment~~ ocean-sediment system in our two simulations, averaged over the last 50 years.

Reservoir	R _{sedbox}	R _{coupled}	Data
DIC	35571 <u>35570</u>	35662 <u>35420</u>	37100 ^a
DOC	650	650	662 ^b
POC	2	2	3 ^a
Sediment POC	< 1	70 <u>130</u>	150 ^c
Sediment calcite	< 1	480 <u>1060</u>	800 ^d
Sediment total	< 1	550 <u>1390</u>	

^a Ciais et al. (2013), pre-industrial estimate

^b Hansell et al. (2009)

^c Emerson and Hedges (1988)

^d Archer (1996)

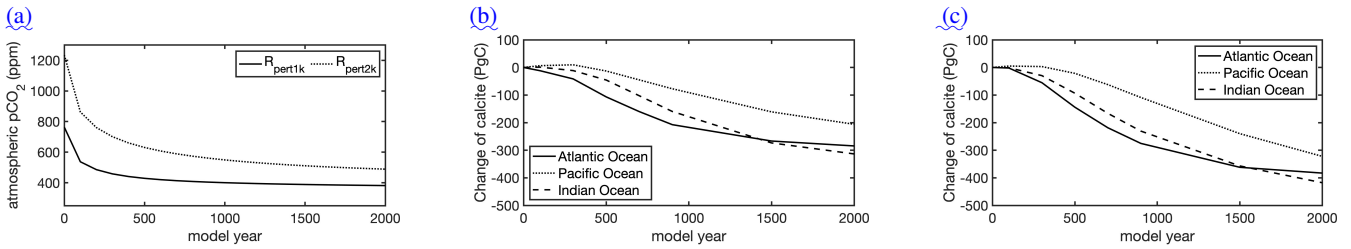


Figure 11. Temporal evolution of the atmospheric pCO₂ in the experiments with an addition of 1000 (R_{pert1k}) and 2000 PgC (R_{pert2k}) in the atmosphere (a); and the change of calcite content in sediments relative to the state before the CO₂ perturbation in R_{pert1k} (b) and R_{pert2k} (c).

3.2.7 Response of the coupled ocean–sediment system to perturbations in atmospheric CO₂

560 In the beginning of the two perturbation experiments R_{pert1k} and R_{pert2k}, 1000 and 2000 PgC were added into the atmosphere, by increasing CO₂ concentrations to 765 and 1235 ppm, respectively (Fig. 11a). The ocean and sediment were initialized from the final state of R_{coupled}.

During the first 250 years, CO₂ concentrations sink rapidly to ~ 480 and 760 ppm, accompanied by a strong increase of DIC and initially a lesser one of alkalinity in the ocean. Afterwards, a much slower decline continues to the end of 2000 years. 565 After 1000 years, about 23% of the added CO₂ remains in the atmosphere in R_{pert1k} and 28% in R_{pert2k}, consistent with the range of 15–30% reported by Archer and Brovkin (2008).

The temporal evolution of sedimentary calcite stocks in the three major ocean basins reflects the carbonate compensation feedback simulated with the coupled ocean–sediment model (Fig. 11b and c). The sedimentary calcite dissolution spreads along the ocean conveyor belt. After the perturbation, inventories quite rapidly start to decline in the Atlantic, followed with 570 some delay by the Indian, while they remain more or less stable in the Pacific Ocean for a few centuries, before they also start to decline there. Losses then get stronger between 250 and 1000 years after the perturbation. By the year 1000 of the simulation, the net dissolution rate has already started to subside, first in the Atlantic and somewhat more slowly in the Indian and Pacific Oceans. At that time, the total carbonate losses from the sediments in R_{pert1k} amount to 220 PgC in the Atlantic, 180 PgC in the Indian, and 90 PgC in the Pacific Ocean (total: 490 PgC); in R_{pert2k} the total loss is 655 PgC with the same partitioning 575 between the ocean basins as in R_{pert1k}. In both experiments, the calcite loss in the Indian Ocean becomes greater than that of the Atlantic Ocean around the year 1500. After 2000 years, the total amounts of calcite dissolved from the seafloor sediments are 800 PgC in R_{pert1k} and 1120 PgC in R_{pert2k}. The sedimentary calcite stock in the Atlantic Ocean seems to near a minimum after 2000 years, while those in the Indian and Pacific Oceans continue to decline.

4 Conclusions

580 This paper documented the coupling of the sediment model MEDUSA2 to the marine biogeochemical model FESOM2.1-REcoM3p-REcoM. The coupling was realized via file exchange, the size of the annual fluxes that exchange material between the bottom of the

ocean and the sedimentary surface, was updated every 50 years. Results from a coupled simulation in a coarse resolution were presented, while a simulation with a much simpler one-layer sediment was used as reference for comparisons.

The simulation with the coupled model reasonably well reproduced the distribution of DIC, Alk, O₂ and nutrients found in observational data products. Biological productivity, deposition rates of particles onto sediments and ~~the related degradation rates and~~ burial fluxes are comparable to estimations made for deep-sea regions (below 1 km water depth), whereas they are underestimated in shallow-water regions (shallower than 10001 m)-km) and in the eastern equatorial Pacific due to the low model resolution ~~used in this study for technical model developments. Simulated quantities in the deep-sea regions (below 1 km water depth) are within or close to the observed ranges.~~

~~While the sediment content of calcite generally agrees well with measurements, the coarse resolution and some missing processes in the ecosystem model lead to some mismatches between simulated and observed sediment content of POC and opal.~~

Nutrient supply from sediments is lower in the coupled simulation than in the simulation with the one-layer sediment, particularly for nitrogen. However, the biological pump is not significantly affected by this decrease, since it is compensated by the additional riverine input of nutrients directly into the surface ocean. Changes in these two sources of nutrients lead to small changes in distribution patterns of diatoms and small phytoplankton. ~~A shift of carbon from the atmosphere to the ocean and sediment reservoir has been found to explain a decrease in atmospheric CO₂ by ~6~~

After 2000 years, atmospheric CO₂ approaches a stable state at the pre-industrial level in our coupled simulation. About 130 ppm between simulations with and without the complex sediment model. PgC is stored in sediments as POC and 1060 PgC as calcite. With a coupled ocean-sediment system the model is able to simulate the carbonate compensation feedback under moderate perturbation of CO₂ in the atmosphere. While most of the conclusions here are robust, one should be aware that the exact changes in the carbon reservoirs and in the rates of deposition and burial presented in this paper are results from a transient state of the simulation, as a period of 2000 years is too short for the ~~atmosphere-ocean-sediment~~ atmosphere-ocean-sediment system to reach ~~the equilibrium. full equilibrium, despite the sediment being pre-charged, i.e.~~ equilibrated with sinking fluxes from an initial ocean model run.

Our model setup which includes MEDUSA2 is being further developed for parallel processing. With that, FESOM2.1-REcoM3p-MEDUSA2 can be run in higher spatial resolution for a better representation of shelf regions. Additionally, a version which includes carbon isotopes is under development. Furthermore, REcoM3p-MEDUSA2 will be used as part of the Earth System Model AWI-ESM2 (Shi et al., 2023) to explore changes in the carbon cycle during the last glacial cycle and feedbacks in the Earth's climate system.

Code and data availability. The source code ~~is available at <https://doi.org/10.5281/zenodo.8315239>.~~ used here has been archived on Zenodo (Ye, 2023, <https://doi.org/10.5281/zenodo.8315239>).

615 *Author contributions.* ~~YY and CV performed the model setup with help from GM, MB and ÖG. YY conducted the simulations and prepared the manuscript with contributions from~~ Conceptualization: YY, CV, GM; Data curation: YY; Formal analysis: YY, CV, GM; Funding acquisition: PK, CV, GM; Investigation: YY; Methodology: YY, CV, GM; Project administration: PK, CV; Software: YY, GM, CV, ÖG, MB; Resources: YY, CV; Supervision: CV, GM, PK; Validation: YY, CV, GM; Visualization: YY; Writing – original draft: YY; Writing – review & editing: YY and all co-authors –

Competing interests. ~~No competing interests are present~~ The authors declare no competing interests.

620 *Acknowledgements.* We thank two anonymous reviewers and the editor for their very constructive comments, which helped to improve the manuscript a lot. YY, PK, CV and MB are supported by the German Federal Ministry of Education and Research (BMBF), as Research for Sustainability initiative (FONA); www.fona.de through the PalMod project (grant number: 01LP1919A). ~~YY~~ YY is additionally supported by the German Research Foundation (DFG) project (grant number: YE 170/2-1). ~~M.B.~~ MB is additionally funded through DFG-ANR project MARCARA. Financial support for GM's work on MEDUSA was provided by the Belgian Fund for Scientific Research – F.R.S.-FNRS (project SERENATA, grant no. CDR J.0123.19). GM is a Research Associate with the Belgian Fund for Scientific Research – F.R.S.-FNRS.
625 JH and ÖG were funded by the Initiative and Networking Fund of the Helmholtz Association (Helmholtz Young Investigator Group Marine Carbon and Ecosystem Feedbacks in the Earth System [MarESys], grant number VH-NG-1301).

References

- Albani, S., Mahowald, N. M., Perry, A. T., Scanza, R. A., Zender, C. S., Heavens, N. G., Maggi, V., Kok, J. F., and Otto-Bliesner, B. L.: Improved Dust Representation in the Community Atmosphere Model, *Journal of Advances in Modeling Earth Systems*, 6, 541–570, <https://doi.org/10.1002/2013MS000279>, 2014.
- 630 Amon, R. and Benner, R.: Rapid cycling of high-molecular-weight dissolved organic matter in the ocean, *Nature*, 369, 549–552, <https://doi.org/10.1038/369549a0>, 1994.
- Andersson, J. H., Wijsman, J. W. M., Herman, P. M. J., Middelburg, J. J., Soetaert, K., and Heip, C.: Respiration patterns in the deep ocean, *Geophysical Research Letters*, 31, L03 304, <https://doi.org/10.1029/2003GL018756>, 2004.
- 635 Archer, D. and Brovkin, V.: The Millennial Atmospheric Lifetime of Anthropogenic CO₂, *Climatic Change*, 90, 283–297, <https://doi.org/10.1007/s10584-008-9413-1>, 2008.
- Archer, D., Kheshgi, H., and Maier-Reimer, E.: Multiple timescales for neutralization of fossil fuel CO₂, *Geophysical Research Letters*, 24, 405–408, <https://doi.org/10.1029/97GL00168>, 1997.
- Archer, D., Eby, M., Brovkin, V., Ridgwell, A., Cao, L., Mikolajewicz, U., Caldeira, K., Matsumoto, K., Munhoven, G., Montenegro, A.,
640 and Tokos, K.: Atmospheric Lifetime of Fossil Fuel Carbon Dioxide, *Annual Review of Earth and Planetary Sciences*, 37, 117–134, <https://doi.org/10.1146/annurev.earth.031208.100206>, 2009.
- Archer, D. E.: An atlas of the distribution of calcium carbonate in sediments of the deep sea, *Global Biogeochemical Cycles*, 10, 159–174, <https://doi.org/10.1029/95GB03016>, 1996.
- Aumont, O., Ethé, C., Tagliabue, A., Bopp, L., and Gehlen, M.: PISCES-v2: An Ocean Biogeochemical Model for Carbon and Ecosystem
645 Studies, *Geoscientific Model Development*, 8, 2465–2513, <https://doi.org/10.5194/gmd-8-2465-2015>, 2015.
- Börker, J., Hartmann, J., Amann, T., Romero-Mujalli, G., Moosdorf, N., and Jenkins, C.: Chemical Weathering of Loess and Its Contribution to Global Alkalinity Fluxes to the Coastal Zone During the Last Glacial Maximum, Mid-Holocene, and Present, *Geochemistry, Geophysics, Geosystems*, 21, e2020GC008922, <https://doi.org/10.1029/2020GC008922>, 2020.
- Broecker, W. S. and Peng, T.-H.: The role of CaCO₃ compensation in the glacial to interglacial atmospheric CO₂ change, *Global Biogeochemical Cycles*, 1, 15–29, 1987.
- 650 Brovkin, V., Ganopolski, A., Archer, D., and Munhoven, G.: Glacial CO₂ cycle as a succession of key physical and biogeochemical processes, *Climate of the Past*, 8, 251–264, <https://doi.org/10.5194/cp-8-251-2012>, 2012.
- Buitenhuis, E. T., Le Quéré, C., Bednaršek, N., and Schiebel, R.: Large Contribution of Pteropods to Shallow CaCO₃ Export, *Global Biogeochemical Cycles*, 33, 458–468, <https://doi.org/10.1029/2018GB006110>, 2019.
- 655 Burdige, D. J.: Preservation of Organic Matter in Marine Sediments: Controls, Mechanisms, and an Imbalance in Sediment Organic Carbon Budgets?, *Chemical Reviews*, 107, 467–485, <https://doi.org/10.1021/cr050347q>, 2007.
- Butzin, M., Ye, Y., Völker, C., Gürses, O., Hauck, J., and Köhler, P.: Carbon isotopes in the marine biogeochemistry model FESOM2.1-RECOM3, *EGU sphere*, 2023, 1–36, <https://doi.org/10.5194/egusphere-2023-1718>, 2023.
- Canfield, D. E., Kristensen, E., and Thamdrup, B.: The Sulfur Cycle, in: *Aquatic Geomicrobiology*, vol. 48 of *Advances in Marine Biology*,
660 pp. 313–381, Elsevier, Amsterdam (NL), [https://doi.org/10.1016/S0065-2881\(05\)48009-8](https://doi.org/10.1016/S0065-2881(05)48009-8), 2005.
- Cartapanis, O., Bianchi, D., Jaccard, S. L., and Galbraith, E. D.: Global pulses of organic carbon burial in deep-sea sediments during glacial maxima, *Nature Communications*, 7, <https://doi.org/10.5194/gmd-2023-68>, 2016.

- Cartapanis, O., Galbraith, E. D., Bianchi, D., and Jaccard, S. L.: Carbon Burial in Deep-Sea Sediment and Implications for Oceanic Inventories of Carbon and Alkalinity over the Last Glacial Cycle, *Clim. Past*, 14, 1819–1850, <https://doi.org/10.5194/cp-14-1819-2018>, 665 2018.
- Christensen, J. P.: Carbon export from continental shelves, denitrification and atmospheric carbon dioxide, *Continental Shelf Research*, 14, 547–576, 1994.
- Christensen, J. P.: A relationship between deep-sea benthic oxygen demand and oceanic primary productivity, *Oceanologica Acta*, 23, 65–82, [https://doi.org/10.1016/S0399-1784\(00\)00101-8](https://doi.org/10.1016/S0399-1784(00)00101-8), 2000.
- 670 Christensen, J. P., Murray, J. W., Devol, A. H., and Codispoti, L. A.: Denitrification in continental shelf sediments has major impact on the oceanic nitrogen budget, *Global Biogeochemical Cycles*, 1, 97–116, 1987.
- Ciais, P., Sabine, C., Bala, G., Bopp, L., Brovkin, V., Canadell, J., Chhabra, A., DeFries, R., Galloway, J., Heimann, M., Jones, C., Quéré, C. L., Myneni, R. B., Piao, S., and Thornton, P.: Carbon and Other Biogeochemical Cycles, in: *Climate Change 2013: The Physical Science Basis. Contribution of Working Group I to the Fifth Assessment Report of the Intergovernmental Panel on Climate Change*, edited by Stocker, T. F., Qin, D., Plattner, G.-K., Tignor, M. M. B., Allen, S. K., Boschung, J., Nauels, A., Xia, Y., Bex, V., and Midgley, P. M., 675 chap. 6, pp. 465–570, Cambridge University Press, https://www.ipcc.ch/site/assets/uploads/2018/02/WG1AR5_Chapter06_FINAL.pdf, 2013.
- Codispoti, L. and Christensen, J.: Nitrification, denitrification and nitrous oxide cycling in the eastern tropical South Pacific Ocean, *Marine chemistry*, 16, 277–300, 1985.
- 680 de Baar, H. J. W. and de Jong, J.: Distributions, Sources and Sinks of Iron in Seawater, in: *The Biogeochemistry of Iron in Seawater*, edited by Turner, D. R. and Hunter, K. A., vol. 7 of *IUPAC Ser. Anal. Phys. Chem. Environ. Syst.*, pp. 123–253, John Wiley & Sons, 2001.
- DeVries, T., Deutsch, C., Rafter, P. A., and Primeau, F.: Marine denitrification rates determined from a global 3-D inverse model, *Biogeo- sciences*, 10, 2481–2496, <https://doi.org/10.5194/bg-10-2481-2013>, 2013.
- Dickson, A. G., Sabine, C. L., and Christian, J. R., eds.: *Guide to Best Practices for Ocean CO₂ Measurements*, vol. 3 of 685 *PICES Special Publication*, Carbon Dioxide Information and Analysis Center, Oak Ridge (TN), https://www.ncei.noaa.gov/access/ocean-carbon-acidification-data-system/oceans/Handbook_2007.html, 2007.
- Dunne, J. P., Sarmiento, J. L., and Gnanadesikan, A.: A synthesis of global particle export from the surface ocean and cycling through the ocean interior and on the seafloor, *Global Biogeochemical Cycles*, 21, GB4006, <https://doi.org/10.1029/2006GB002907>, 2007.
- Dunne, J. P., Hales, B., and Toggweiler, J. R.: Global calcite cycling constrained by sediment preservation controls, *Global Biogeochemical* 690 *Cycles*, 26, GB3023, <https://doi.org/10.1029/2010GB003935>, 2012.
- Elrod, V. A., Berelson, W. M., Coale, K. H., and Johnson, K. S.: The flux of iron from continental shelf sediments: A missing source for global budgets, *Geophysical Research Letters*, 31, <https://doi.org/10.1029/2004GL020216>, 2004.
- Emerson, S. and Hedges, J. I.: Processes controlling the organic carbon content of open ocean sediments, *Paleoceanography*, 3, 621–634, <https://doi.org/10.1029/PA003i005p00621>, 1988.
- 695 Friedlingstein, P., O’Sullivan, M., Jones, M. W., Andrew, R. M., Gregor, L., Hauck, J., Le Quéré, C., Luijckx, I. T., Olsen, A., Peters, G. P., Peters, W., Pongratz, J., Schwingshackl, C., Sitch, S., Canadell, J. G., Ciais, P., Jackson, R. B., Alin, S. R., Alkama, R., Arneeth, A., Arora, V. K., Bates, N. R., Becker, M., Bellouin, N., Bittig, H. C., Bopp, L., Chevallier, F., Chini, L. P., Cronin, M., Evans, W., Falk, S., Feely, R. A., Gasser, T., Gehlen, M., Gkritzalis, T., Gloege, L., Grassi, G., Gruber, N., Gürses, Ö., Harris, I., Hefner, M., Houghton, R. A., Hurtt, G. C., Iida, Y., Ilyina, T., Jain, A. K., Jersild, A., Kadono, K., Kato, E., Kennedy, D., Klein Goldewijk, K., Knauer, J., Korsbakken, J. I., 700 Landschützer, P., Lefèvre, N., Lindsay, K., Liu, J., Liu, Z., Marland, G., Mayot, N., McGrath, M. J., Metz, N., Monacchi, N. M., Munro,

- D. R., Nakaoka, S.-I., Niwa, Y., O'Brien, K., Ono, T., Palmer, P. I., Pan, N., Pierrot, D., Pockock, K., Poulter, B., Resplandy, L., Robertson, E., Rödenbeck, C., Rodriguez, C., Rosan, T. M., Schwinger, J., Séférian, R., Shutler, J. D., Skjelvan, I., Steinhoff, T., Sun, Q., Sutton, A. J., Sweeney, C., Takao, S., Tanhua, T., Tans, P. P., Tian, X., Tian, H., Tilbrook, B., Tsujino, H., Tubiello, F., van der Werf, G. R., Walker, A. P., Wanninkhof, R., Whitehead, C., Willstrand Wranne, A., Wright, R., Yuan, W., Yue, C., Yue, X., Zaehle, S., Zeng, J., and Zheng, B.:
705 Global Carbon Budget 2022, *Earth System Science Data*, 14, 4811–4900, <https://doi.org/10.5194/essd-14-4811-2022>, 2022.
- Garcia, H. E., Locarnini, R. A., Boyer, T. P., Antonov, J. I., Baranova, O. K., Zweng, M. M., Reagan, J. R., and Johnson, D. R.: *World Ocean Atlas 2013, Volume 4: Dissolved Inorganic Nutrients (Phosphate, Nitrate, Silicate)*. S. Levitus, Ed., A. Mishonov Technical Ed., Tech. rep., NOAA Atlas NESDIS 76, 2014.
- Garcia, H. E., Weathers, K. W., Paver, C. R., Smolyar, I., Boyer, T. P., Locarnini, R. A., Zweng, M. M., Mishonov, A. V., Baranova,
710 O. K., Seidov, D., and Reagan, J. R.: *World Ocean Atlas 2018, Volume 3: Dissolved Oxygen, Apparent Oxygen Utilization, and Oxygen Saturation*. A. Mishonov Technical Editor, Tech. rep., NOAA Atlas NESDIS 83, 2019.
- Glud, R. N.: Oxygen dynamics of marine sediments, *Marine Biology Research*, 4, 243–289, <https://doi.org/10.1080/17451000801888726>, 2008.
- Guieu, C., Huang, W. W., Martin, J.-M., and Yong, Y. Y.: Outflow of trace metals into the Laptev Sea by the Lena River, *Marine Chemistry*,
715 53, 255–267, [https://doi.org/10.1016/0304-4203\(95\)00093-3](https://doi.org/10.1016/0304-4203(95)00093-3), 1996.
- Gürses, O., Oziel, L., Karakuş, O., Sidorenko, D., Völker, C., Ye, Y., Zeising, M., Butzin, M., and Hauck, J.: Ocean biogeochemistry in the coupled ocean–sea ice–biogeochemistry model FESOM2.1–REcoM3, *Geoscientific Model Development*, 16, 4883–4936, <https://doi.org/10.5194/gmd-16-4883-2023>, 2023.
- Hansell, D. A., Carlson, C. A., Repeta, D. J., and Schlitzer, R.: Dissolved Organic Matter in the Ocean : A Controversy Stimulates New
720 Insights, *Oceanography*, 22, <https://doi.org/10.5670/oceanog.2009.109>, 2009.
- Hattori, A.: Denitrification and dissimilatory nitrate reduction, in: *Nitrogen in the marine environment*, edited by Carpenter, E. J. and Capone, D. G., chap. 6, pp. 191–232, Academic Press, New York (NY), 1 edn., 1983.
- Hayes, C. T., Costa, K. M., Anderson, R. F., Calvo, E., Chase, Z., Demina, L. L., Dutay, J.-C., German, C. R., Heimbürger-Boavida, L.-E., Jaccard, S. L., Jacobel, A., Kohfeld, K. E., Kravchishina, M. D., Lippold, J., Mekik, F., Missiaen, L., Pavia, F. J., Paytan, A., Pedrosa-
725 Pamies, R., Petrova, M. V., Rahman, S., Robinson, L. F., Roy-Barman, M., Sanchez-Vidal, A., Shiller, A., Tagliabue, A., Tessin, A. C., Van Hulten, M., and Zhang, J.: Global Ocean Sediment Composition and Burial Flux in the Deep Sea, *Global Biogeochemical Cycles*, 35, e2020GB006769, <https://doi.org/10.1029/2020GB006769>, 2021.
- Heinze, C., Maier-Reimer, E., Winguth, A. M. E., and Archer, D.: A Global Oceanic Sediment Model for Long-Term Climate Studies, *Global Biogeochemical Cycles*, 13, 221–250, <https://doi.org/10.1029/98GB02812>, 1999.
- 730 Hilton, R. G. and West, A. J.: Mountains, erosion and the carbon cycle, *Nature Reviews Earth and Environment*, 1, <https://doi.org/10.1038/s43017-020-0058-6>, 2020.
- Himstedt, K.: Multiple Execution of the Same MPI Application to Exploit Parallelism at Hotspots with Minimal Code Changes: A Case Study with FESOM2-Iceberg and FESOM2-REcoM, *EGUsphere*, 2023, 1–27, <https://doi.org/10.5194/egusphere-2023-756>, 2023.
- Hohn, S.: Coupling and decoupling of biogeochemical cycles in marine ecosystems, Ph.D. thesis, Universität Bremen, Fachbereich Biologie,
735 2009.
- Jahnke, R. A.: The global ocean flux of particulate organic carbon: Areal distribution and magnitude, *Global Biogeochemical Cycles*, 10, 71–88, <https://doi.org/10.1029/95GB03525>, 1996.

- Jørgensen, B. B.: Processes at the sediment-water interface, in: *The Major Biogeochemical Cycles and Their Interactions*, edited by Bolin, B. and Cook, R. B., vol. 21 of *SCOPE Reports*, pp. 477–509, John Wiley and Sons, New York (NY), 1983.
- 740 Jørgensen, B. B. and Kasten, S.: Sulfur Cycling and Methane Oxidation, in: *Marine Geochemistry*, edited by Schulz, H. D. and Zabel, M., chap. 8, pp. 271–309, Springer-Verlag, Berlin, Heidelberg (DE), https://doi.org/10.1007/3-540-32144-6_8, 2006.
- Jørgensen, B. B., Wenzhöfer, F., Egger, M., and Glud, R. N.: Sediment oxygen consumption: Role in the global marine carbon cycle, *Earth-Science Reviews*, 228, 103 987, <https://doi.org/10.1016/j.earscirev.2022.103987>, 2022.
- Keppler, L., Landschützer, P., Gruber, N., Lauvset, S. K., and Stemmler, I.: Seasonal Carbon Dynamics in the Near-Global Ocean, *Global Biogeochemical Cycles*, 34, e2020GB006571, <https://doi.org/10.1029/2020GB006571>, 2020.
- 745 Knecht, N. S., Benedetti, F., Hofmann Elizondo, U., Bednaršek, N., Chaabane, S., de Weerd, C., Peijnenburg, K. T. C. A., Schiebel, R., and Vogt, M.: The Impact of Zooplankton Calcifiers on the Marine Carbon Cycle, *Global Biogeochemical Cycles*, 37, e2022GB007685, <https://doi.org/10.1029/2022GB007685>, 2023.
- Köhler, P.: Anthropogenic CO₂ of high emission scenario compensated after 3500 years of ocean alkalization with an annually constant dissolution of 5 Pg of olivine, *Frontiers in Climate*, 2, 575744, <https://doi.org/10.3389/fclim.2020.575744>, 2020.
- 750 Köhler, P. and Munhoven, G.: Late Pleistocene carbon cycle revisited by considering solid Earth processes, *Paleoceanography and Paleoclimatology*, 35, e2020PA004020, <https://doi.org/10.1029/2020PA004020>, 2020.
- Krachler, R., Jirsa, F., and Ayromlou, S.: Factors influencing the dissolved iron input by river water to the open ocean, *Biogeosciences*, 2, 311–315, <https://doi.org/10.5194/bg-2-311-2005>, 2005.
- 755 Kriest, I. and Oeschler, A.: Swept under the Carpet: Organic Matter Burial Decreases Global Ocean Biogeochemical Model Sensitivity to Remineralization Length Scale, *Biogeosciences*, 10, 8401–8422, <https://doi.org/10.5194/bg-10-8401-2013>, 2013.
- Kurahashi-Nakamura, T., Paul, A., Munhoven, G., Merkel, U., and Schulz, M.: Coupling of a Sediment Diagenesis Model (MEDUSA) and an Earth System Model (CESM1.2): A Contribution toward Enhanced Marine Biogeochemical Modelling and Long-Term Climate Simulations, *Geoscientific Model Development*, 13, 825–840, <https://doi.org/10.5194/gmd-13-825-2020>, 2020.
- 760 Lan, X., Tans, P., and K.W., T.: Trends in globally-averaged CO₂ determined from NOAA Global Monitoring Laboratory measurements. Version 2023-06, <https://doi.org/10.15138/9N0H-ZH07>, 2023.
- Large, W. G. and Yeager, S. G.: The Global Climatology of an Interannually Varying Air-Sea Flux Data Set, *Climate Dynamics*, 33, 341–364, <https://doi.org/10.1007/s00382-008-0441-3>, 2009.
- Lauvset, S. K., Key, R. M., Olsen, A., van Heuven, S., Velo, A., Lin, X., Schirnick, C., Kozyr, A., Tanhua, T., Hoppema, M., Jutterström, S., Steinfeldt, R., Jeansson, E., Ishii, M., Perez, F. F., Suzuki, T., and Watelet, S.: A New Global Interior Ocean Mapped Climatology: The 1 × 1 GLODAP Version 2, *Earth System Science Data*, 8, 325–340, <https://doi.org/10.5194/essd-8-325-2016>, 2016.
- 765 Liu, K.-K. and Kaplan, I. R.: Denitrification rates and availability of organic matter in marine environments, *Earth and Planetary Science Letters*, 68, 88–100, 1984.
- Martin, J. H., Knauer, G. A., Karl, D. M., and Broenkow, W. W.: VERTEX: carbon cycling in the northeast Pacific, *Deep Sea Research Part A. Oceanographic Research Papers*, 34, 267–285, [https://doi.org/10.1016/0198-0149\(87\)90086-0](https://doi.org/10.1016/0198-0149(87)90086-0), 1987.
- 770 Meinshausen, M., Smith, S. J., Calvin, K., Daniel, J. S., Kainuma, M. L., Lamarque, J.-F., Matsumoto, K., Montzka, S. A., Raper, S. C., Riahi, K., et al.: The RCP greenhouse gas concentrations and their extensions from 1765 to 2300, *Climatic change*, 109, 213–241, 2011.
- Meinshausen, M., Vogel, E., Nauels, A., Lorbacher, K., Meinshausen, N., Etheridge, D., Fraser, P., Montzka, S. A., Rayner, P., Trudinger, C., Krummel, P., Beyerle, U., Cannadell, J. G., Daniel, J. S., Enting, I., Law, R. M., O’Doherty, S., Prinn, R. G., Reimann, S., Rubino, M.,

- 775 Velders, G. J. M., Vollmer, M. K., and Weiss, R.: Historical greenhouse gas concentrations for climate modelling (CMIP6), *Geoscientific Model Development*, 10, 2057–2116, <https://doi.org/10.5194/gmd-10-2057-2017>, 2017.
- Middelburg, J. J., Soetaert, K., Herman, P. M. J., and Heip, C. H. R.: Denitrification in marine sediments: A model study, *Global Biogeochemical Cycles*, 10, 661–673, <https://doi.org/10.1029/96GB02562>, 1996.
- Middelburg, J. J., Soetaert, K., and Herman, P. M. J.: Empirical relationships for use in global diagenetic models, *Deep Sea Research Part I: Oceanographic Research Papers*, 44, 327–344, [https://doi.org/10.1016/S0967-0637\(96\)00101-X](https://doi.org/10.1016/S0967-0637(96)00101-X), 1997.
- 780 Milliman, J. D. and Meade, R. H.: World-wide delivery of river sediment to the oceans, *JGeol*, 91, 1–21, <https://doi.org/10.1086/628741>, 1983.
- Moreira Martinez, S., Roche, D. M., Munhoven, G., and Waelbroeck, C.: Coupling MEDUSA sediment model to iLOVECLIM (v1.1 β) Earth system model, in: 12th International Conference on Paleoceanography (ICP12), pp. P–368, Utrecht (NL), <http://icp12.uu.nl/wp-content/uploads/2016/08/Poster-abstracts-sessie-3.pdf>, 2016.
- 785 Muller-Karger, F. E., Varela, R., Thunell, R., Luers sen, R., Hu, C., and Walsh, J. J.: The importance of continental margins in the global carbon cycle, *Geophysical Research Letters*, 32, L01602, <https://doi.org/10.1029/2004GL021346>, 2005.
- Munhoven, G.: Glacial–Interglacial Rain Ratio Changes: Implications for Atmospheric and Ocean–Sediment Interaction, *Deep Sea Research Part II: Topical Studies in Oceanography*, 54, 722–746, <https://doi.org/10.1016/j.dsr2.2007.01.008>, 2007.
- 790 Munhoven, G.: Model of Early Diagenesis in the Upper Sediment with Adaptable Complexity – MEDUSA (v. 2): A Time-Dependent Biogeochemical Sediment Module for Earth System Models, *Process Analysis and Teaching, Geoscientific Model Development*, 14, 3603–3631, <https://doi.org/10.5194/gmd-14-3603-2021>, 2021.
- Nelson, D. M., Tréguer, P., Brzezinski, M. A., Leynaert, A., and Qu’eguiner, B.: Production and dissolution of biogenic silica in the ocean: Revised global estimates, comparison with regional data and relationship to biogenic sedimentation, *Global Biogeochemical Cycles*, 9, 359–372, <https://doi.org/10.1029/95GB01070>, 1995.
- 795 Parameswaran, N., González, E., Burwicz-Galerie, E., Braack, M., and Wallmann, K.: NN-TOC v1: global prediction of total organic carbon in marine sediments using deep neural networks, *EGUsphere* [preprint], <https://doi.org/10.5194/egusphere-2024-1360>, 2024.
- Peucker-Ehrenbrink, B.: Land2Sea database of river drainage basin sizes, annual water discharges, and suspended sediment fluxes, *Geochemistry, Geophysics, Geosystems*, 10, <https://doi.org/10.1029/2008GC002356>, 2009.
- 800 Picard, A., Davis, R. S., Gläser, M., and Fujii, K.: Revised formula for the density of moist air (CIPM-2007), *Metrologia*, 45, 149–155, <https://doi.org/10.1088/0026-1394/45/2/004>, 2008.
- Sarmiento, J. L. and Gruber, N.: *Ocean Biogeochemical Dynamics*, Princeton University Press, <https://doi.org/10.2307/j.ctt3fgxqx>, 2006.
- Sarmiento, J. L., Dunne, J., Gnanadesikan, A., Key, R. M., Matsumoto, K., and Slater, R.: A new estimate of the CaCO₃ to organic carbon export ratio, *Global Biogeochemical Cycles*, 16, 1107, <https://doi.org/10.1029/2002GB001919>, 2002.
- 805 Schartau, M., Engel, A., Schröter, J., Thoms, S., Völker, C., and Wolf-Gladrow, D.: Modelling carbon overconsumption and the formation of extracellular particulate organic carbon, *Biogeosciences*, 4, 433–454, <https://doi.org/10.5194/bg-4-433-2007>, 2007.
- Scholz, P., Sidorenko, D., Gurses, O., Danilov, S., Koldunov, N., Wang, Q., Sein, D., Smolentseva, M., Rakowsky, N., and Jung, T.: Assessment of the Finite-volumE Sea Ice-Ocean Model (FESOM2.0) – Part 1: Description of Selected Key Model Elements and Comparison to Its Predecessor Version, *Geoscientific Model Development*, 12, 4875–4899, <https://doi.org/10.5194/gmd-12-4875-2019>, 2019.
- 810 Scholz, P., Sidorenko, D., Danilov, S., Wang, Q., Koldunov, N., Sein, D., and Jung, T.: Assessment of the Finite-VolumE Sea Ice–Ocean Model (FESOM2.0) – Part 2: Partial Bottom Cells, Embedded Sea Ice and Vertical Mixing Library CVMix, *Geoscientific Model Development*, 15, 335–363, <https://doi.org/10.5194/gmd-15-335-2022>, 2022.

- Séférian, R., Berthet, S., Yool, A., Palmiéri, J., Bopp, L., Tagliabue, A., Kwiatkowski, L., Aumont, O., Christian, J., Dunne, J., Gehlen, M., Ilyina, T., John, J. G., Li, H., Long, M. C., Luo, J. Y., Nakano, H., Romanou, A., Schwinger, J., Stock, C., Santana-Falcón, Y., Takano, Y., Tjiputra, J., Tsujino, H., Watanabe, M., Wu, T., Wu, F., and Yamamoto, A.: Tracking Improvement in Simulated Marine Biogeochemistry Between CMIP5 and CMIP6, *Current Climate Change Reports*, 6, 95–119, <https://doi.org/10.1007/s40641-020-00160-0>, 2020.
- 815 Seifert, M., Nissen, C., Rost, B., and Hauck, J.: Cascading effects augment the direct impact of CO₂ on phytoplankton growth in a biogeochemical model, *Elementa: Science of the Anthropocene*, 10, 00 104, <https://doi.org/10.1525/elementa.2021.00104>, 2022.
- Seiter, K., Hensen, C., Schröter, J., and Zabel, M.: Organic Carbon Content in Surface Sediments — Defining Regional Provinces, *Deep Sea Research Part I: Oceanographic Research Papers*, 51, 2001–2026, <https://doi.org/10.1016/j.dsr.2004.06.014>, 2004.
- 820 Seiter, K., Hensen, C., and Zabel, M.: Benthic carbon mineralization on a global scale, *Global Biogeochemical Cycles*, 19, <https://doi.org/10.1029/2004GB002225>, 2005.
- Shi, X., Cauquoin, A., Lohmann, G., Jonkers, L., Wang, Q., Yang, H., Sun, Y., and Werner, M.: Simulated stable water isotopes during the mid-Holocene and pre-industrial using AWI-ESM-2.1-wiso, *Geoscientific Model Development Discussions*, 2023, 1–39, <https://doi.org/10.5194/gmd-2023-68>, 2023.
- 825 Smith, S. V. and Hollibaugh, J. T.: Coastal Metabolism and the Oceanic Organic Carbon Balance, *Reviews of Geophysics*, 31, 75–89, <https://doi.org/10.1029/92RG02584>, 1993.
- Snelgrove, P. V., Soetaert, K., Solan, M., Thrush, S., Wei, C.-L., Danovaro, R., Fulweiler, R. W., Kitazato, H., Ingole, B., Norkko, A., Parkes, R. J., and Volkenborn, N.: Global Carbon Cycling on a Heterogeneous Seafloor, *Trends in Ecology & Evolution*, 33, 96–105, <https://doi.org/10.1016/j.tree.2017.11.004>, 2018.
- 830 Soetaert, K., Herman, P. M. J., and Middelburg, J. J.: A model of early diagenetic processes from the shelf to abyssal depths, *Geochimica Cosmochimica Acta*, 60, 1019–1040, [https://doi.org/10.1016/0016-7037\(96\)00013-0](https://doi.org/10.1016/0016-7037(96)00013-0), 1996.
- Steele, M., Morley, R., and Ermold, W.: PHC: A Global Ocean Hydrography with a High-Quality Arctic Ocean, *Journal of Climate*, 14, 2079–2087, [https://doi.org/10.1175/1520-0442\(2001\)014<2079:PAGOHW>2.0.CO;2](https://doi.org/10.1175/1520-0442(2001)014<2079:PAGOHW>2.0.CO;2), 2001.
- 835 Stratmann, T., Wei, C.-L., Lin, Y.-S., and van Oevelen, D.: The SCOC database, a large, open, and global database with sediment community oxygen consumption rates, *Scientific Data*, 6, <https://doi.org/10.1038/s41597-019-0259-3>, 2019.
- Thullner, M., Dale, A. W., and Regnier, P.: Global-scale quantification of mineralization pathways in marine sediments: A reaction-transport modeling approach, *Geochemistry, Geophysics, Geosystems*, 10, Q10012, <https://doi.org/https://doi.org/10.1029/2009GC002484>, 2009.
- Tréguer, P., Nelson, D. M., Bennekou, A. J. V., DeMaster, D. J., Leynaert, A., and Quéguiner, B.: The Silica Balance in the World Ocean: A Reestimate, *Science*, 268, 375–379, <https://doi.org/10.1126/science.268.5209.375>, 1995.
- 840 Tréguer, P. J. and De La Rocha, C. L.: The World Ocean Silica Cycle, *Annual Review of Marine Science*, 5, 477–501, <https://doi.org/10.1146/annurev-marine-121211-172346>, 2013.
- Tréguer, P. J., Sutton, J. N., Brzezinski, M., Charette, M. A., Devries, T., Dutkiewicz, S., Ehlert, C., Hawkings, J., Leynaert, A., Liu, S. M., Llopis Monferrer, N., López-Acosta, M., Maldonado, M., Rahman, S., Ran, L., and Rouxel, O.: Reviews and Syntheses: The Biogeochemical Cycle of Silicon in the Modern Ocean, *Biogeosciences*, 18, 1269–1289, <https://doi.org/10.5194/bg-18-1269-2021>, 2021.
- 845 Trenberth, K. E. and Smith, L.: The Mass of the Atmosphere: A Constraint on Global Analyses, *Journal of Climate*, 18, 864–875, <https://doi.org/10.1175/JCLI-3299.1>, 2005.
- Volk, T. and Hoffert, M. I.: Ocean Carbon Pumps : Analysis of Relative Strengths and Efficiencies in Ocean-Driven Atmospheric CO₂ Changes, in: *The Carbon Cycle and Atmospheric CO₂ : Natural Variations Archean to Present*, edited by Sundquist, E. T. and

- 850 Broecker, W. S., vol. 32 of *Geophysical Monograph Series*, pp. 99–110, American Geophysical Union (AGU), Washington (DC),
<https://doi.org/10.1029/GM032p0099>, 1985.
- Wanninkhof, R.: Relationship between wind speed and gas exchange over the ocean revisited, *Limnology and Oceanography: Methods*, 12,
351–362, <https://doi.org/10.4319/lom.2014.12.351>, 2014.
- Ye, Y.: Ocean biogeochemistry model FESOM2.1-REcoM3 coupled with a sediment model MEDUSA2, Zenodo [software],
855 <https://doi.org/10.5281/zenodo.8315240>, 2023.
- Zeebe, R. E. and Wolf-Gladrow, D. A.: CO₂ in Seawater: Equilibrium, Kinetics, Isotopes, vol. 65 of *Elsevier Oceanography Book Series*,
Elsevier Science Publishing, Amsterdam, The Netherlands, 2001.

Appendix A: Figures

~~Clay flux at sediment–water interface (-):~~

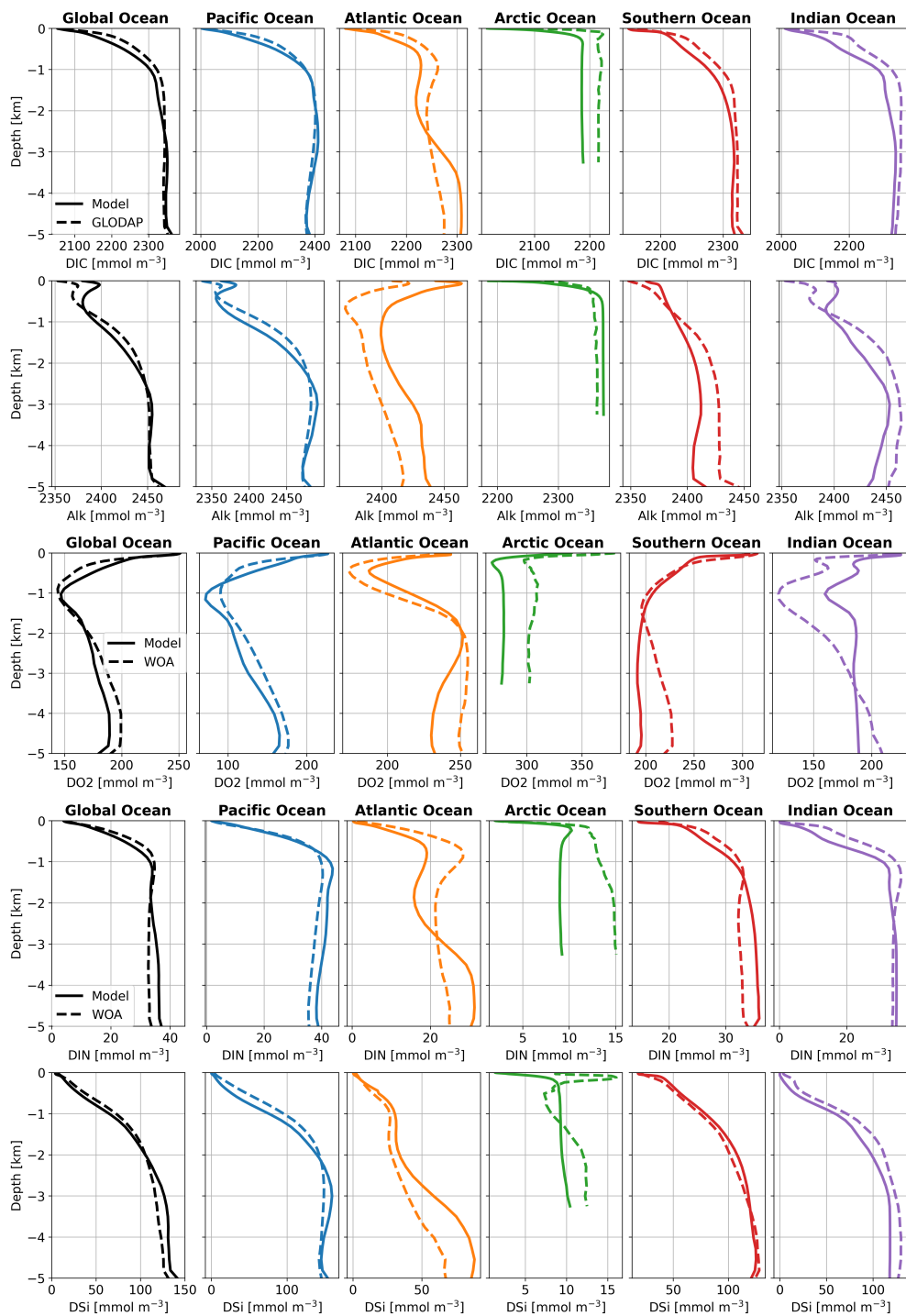


Figure A1. Averaged vertical profiles of DIC, Alk, O_2 , DIN and DSi in ocean basins (mmol m^{-3}) in [RecoopedR_{spring}](#), compared with [GLODAP-GLODAPv2 \(Large and Yeager, 2009\)](#) and [WOA data \(Garcia et al., 2019\)](#) which were used as initial conditions in simulations in this study.

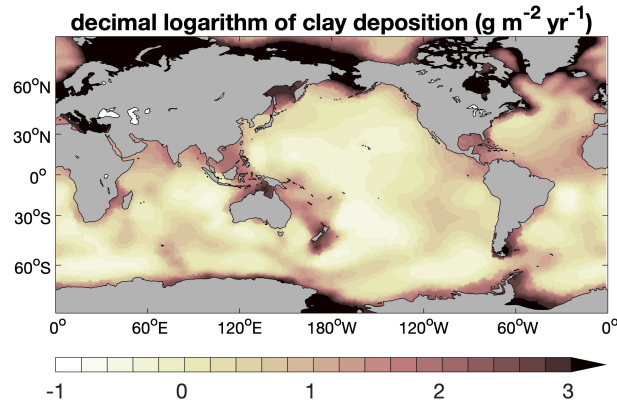


Figure B1. Decimal logarithm of clay flux at sediment–water interface ($\text{g m}^{-2} \text{yr}^{-1}$).

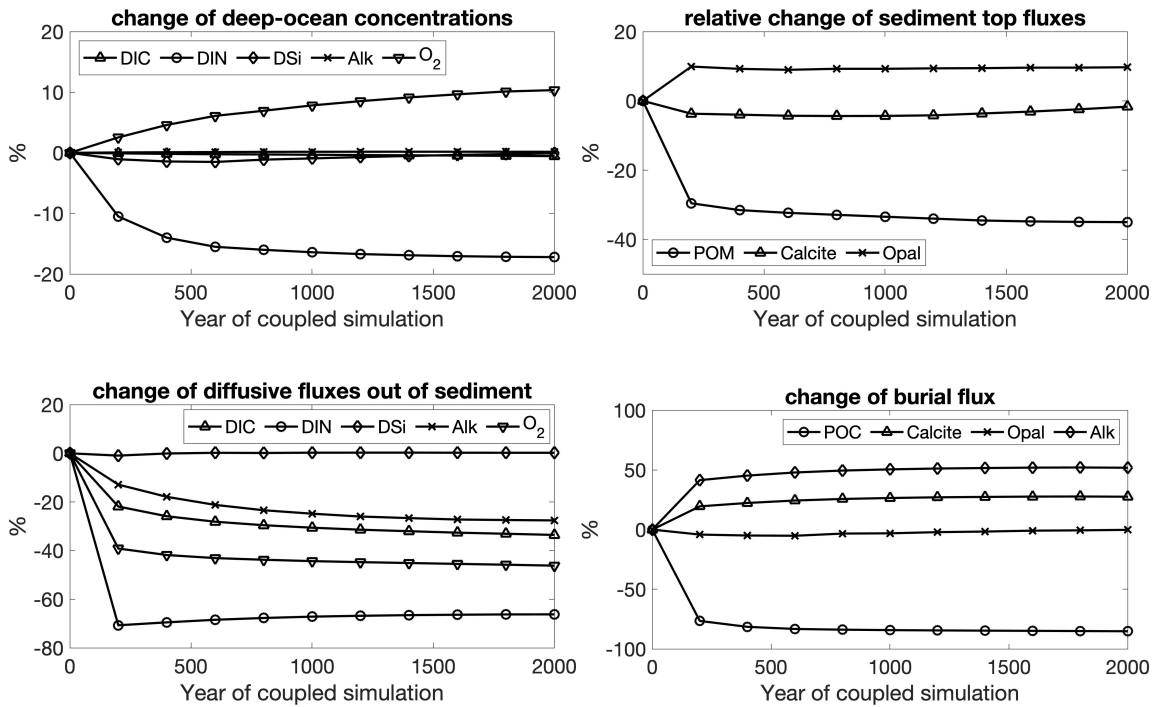


Figure C1. Temporal changes of deep ocean concentrations (DIC, DIN, DSi, Alk and $\Theta_2\text{O}_2$) (upper left) and their diffusive fluxes out of sediments (lower left); deposition rates of POM, calcite and opal onto sediment top (upper right) diffusive fluxes of solutes out of sediments (lower-left) and their burial fluxes (lower right) during the 2000-year coupled simulation R_{coupled} . Changes are in percentages relative to the values at the beginning of R_{coupled} .

D1 FESOM2.1-REcoM3p

D1 MEDUSA2

Reaction rate law expressions and parameter values used for the early diagenetic reaction network in MEDUSA2. C_{cs} is the concentration in seawater at saturation with respect to calcite. $(\dots)^+$ denotes the positive part of (\dots) . C_{hoxI} and C_{hoxI} are the half-saturation concentrations of for the oxie remineralisation of the organic organic matter classes and, resp. C_{hnrI} is the half-saturation concentration of and C_{ioI} the characteristic inhibition concentration of for the oxidation of by nitrate reduction and similarly C_{hnr2} and C_{io2} are the respective constants for. Concentrations of solids are expressed in, those of solutes in; the different reaction rates, \hat{R} , are expressed in terms of the dissolving/remineralised solid, in. Calcite dissolution $\hat{R}_{\text{cdis}} = k_c (1 - \varphi) [\text{Calcite}] ((1 - [\text{CO}_3^{2-}]/C_{cs})^+)^{4.5}$ with $k_c = 365.25 \text{ yr}^{-1} (= 1 \text{ day}^{-1})$, $C_{cs} = C_{cs}(S, T, p)$ Oxie remineralisation $\hat{R}_{\text{omIox}} = k_{\text{oxI}} (1 - \varphi) [\text{POM}_1] ([\text{O}_2]/(C_{\text{hoxI}} + [\text{O}_2]))$ with $k_{\text{oxI}} = 0.32 \text{ yr}^{-1}$, $C_{\text{hoxI}} = 20 \mu\text{mol L}^{-1}$ remin. by nitrate reduction $\hat{R}_{\text{omInr}} = k_{\text{nrI}} (1 - \varphi) [\text{POM}_1] ([\text{NO}_3^-]/(C_{\text{hnrI}} + [\text{NO}_3^-])) (C_{\text{ioI}}/(C_{\text{ioI}} + [\text{O}_2]))$ with $k_{\text{nrI}} = 0.0032 \text{ yr}^{-1}$, $C_{\text{hnrI}} = 5 \mu\text{mol L}^{-1}$, $C_{\text{ioI}} = 20 \mu\text{mol L}^{-1}$ Oxie remineralisation $\hat{R}_{\text{om2ox}} = k_{\text{ox2}} (1 - \varphi) [\text{POM}_2] ([\text{O}_2]/(C_{\text{hox2}} + [\text{O}_2]))$ with $k_{\text{ox2}} = 0.032 \text{ yr}^{-1}$, $C_{\text{hox2}} = 20 \mu\text{mol L}^{-1}$ remin. by nitrate reduction $\hat{R}_{\text{om2nr}} = k_{\text{nr2}} (1 - \varphi) [\text{POM}_2] ([\text{NO}_3^-]/(C_{\text{hnr2}} + [\text{NO}_3^-])) (C_{\text{io2}}/(C_{\text{io2}} + [\text{O}_2]))$ with $k_{\text{nr2}} = 0.0032 \text{ yr}^{-1}$, $C_{\text{hnr2}} = 5 \mu\text{mol L}^{-1}$, $C_{\text{io2}} = 20 \mu\text{mol L}^{-1}$ Opal dissolution $\hat{R}_{\text{odis}} = k_o (1 - \varphi) [\text{Opal}] (C_{\text{os}} - [\text{H}_4\text{SiO}_4])^+$ with $k_o = 0.03 \text{ yr}^{-1} \text{ mol}^{-1} \text{ m}^3$, $C_{\text{os}} = 1000 \mu\text{mol L}^{-1}$ in Gürses et al. (2023).

D1 MEDUSA2

Reaction rate law expressions and parameter values used for the early diagenetic reaction network in MEDUSA2. C_{cs} is the concentration in seawater at saturation with respect to calcite. $(\dots)^+$ denotes the positive part of (\dots) . C_{hoxI} and C_{hoxI} are the half-saturation concentrations of for the oxie remineralisation of the organic organic matter classes and, resp. C_{hnrI} is the half-saturation concentration of and C_{ioI} the characteristic inhibition concentration of for the oxidation of by nitrate reduction and similarly C_{hnr2} and C_{io2} are the respective constants for. Concentrations of solids are expressed in, those of solutes in; the different reaction rates, \hat{R} , are expressed in terms of the dissolving/remineralised solid, in. Calcite dissolution $\hat{R}_{\text{cdis}} = k_c (1 - \varphi) [\text{Calcite}] ((1 - [\text{CO}_3^{2-}]/C_{cs})^+)^{4.5}$ with $k_c = 365.25 \text{ yr}^{-1} (= 1 \text{ day}^{-1})$, $C_{cs} = C_{cs}(S, T, p)$ Oxie remineralisation $\hat{R}_{\text{omIox}} = k_{\text{oxI}} (1 - \varphi) [\text{POM}_1] ([\text{O}_2]/(C_{\text{hoxI}} + [\text{O}_2]))$ with $k_{\text{oxI}} = 0.32 \text{ yr}^{-1}$, $C_{\text{hoxI}} = 20 \mu\text{mol L}^{-1}$ remin. by nitrate reduction $\hat{R}_{\text{omInr}} = k_{\text{nrI}} (1 - \varphi) [\text{POM}_1] ([\text{NO}_3^-]/(C_{\text{hnrI}} + [\text{NO}_3^-])) (C_{\text{ioI}}/(C_{\text{ioI}} + [\text{O}_2]))$ with $k_{\text{nrI}} = 0.0032 \text{ yr}^{-1}$, $C_{\text{hnrI}} = 5 \mu\text{mol L}^{-1}$, $C_{\text{ioI}} = 20 \mu\text{mol L}^{-1}$ Oxie remineralisation $\hat{R}_{\text{om2ox}} = k_{\text{ox2}} (1 - \varphi) [\text{POM}_2] ([\text{O}_2]/(C_{\text{hox2}} + [\text{O}_2]))$ with $k_{\text{ox2}} = 0.032 \text{ yr}^{-1}$, $C_{\text{hox2}} = 20 \mu\text{mol L}^{-1}$ remin. by nitrate reduction $\hat{R}_{\text{om2nr}} = k_{\text{nr2}} (1 - \varphi) [\text{POM}_2] ([\text{NO}_3^-]/(C_{\text{hnr2}} + [\text{NO}_3^-])) (C_{\text{io2}}/(C_{\text{io2}} + [\text{O}_2]))$ with $k_{\text{nr2}} = 0.0032 \text{ yr}^{-1}$, $C_{\text{hnr2}} = 5 \mu\text{mol L}^{-1}$, $C_{\text{io2}} = 20 \mu\text{mol L}^{-1}$ Opal dissolution $\hat{R}_{\text{odis}} = k_o (1 - \varphi) [\text{Opal}] (C_{\text{os}} - [\text{H}_4\text{SiO}_4])^+$ with $k_o = 0.03 \text{ yr}^{-1} \text{ mol}^{-1} \text{ m}^3$, $C_{\text{os}} = 1000 \mu\text{mol L}^{-1}$ in Gürses et al. (2023). **Table D1.** Parameters in REcoM3 modified in this study compared to Gürses et al. (2023). *Vcalc* replaces 0.0288 in Eq. in Eq. A29 in Gürses et al. (2023).

D1 MEDUSA2

Reaction rate law expressions and parameter values used for the early diagenetic reaction network in MEDUSA2. C_{cs} is the concentration in seawater at saturation with respect to calcite. $(\dots)^+$ denotes the positive part of (\dots) . C_{hoxI} and C_{hoxI} are the half-saturation concentrations of for the oxie remineralisation of the organic organic matter classes and, resp. C_{hnrI} is the half-saturation concentration of and C_{ioI} the characteristic inhibition concentration of for the oxidation of by nitrate reduction and similarly C_{hnr2} and C_{io2} are the respective constants for. Concentrations of solids are expressed in, those of solutes in; the different reaction rates, \hat{R} , are expressed in terms of the dissolving/remineralised solid, in. Calcite dissolution $\hat{R}_{\text{cdis}} = k_c (1 - \varphi) [\text{Calcite}] ((1 - [\text{CO}_3^{2-}]/C_{cs})^+)^{4.5}$ with $k_c = 365.25 \text{ yr}^{-1} (= 1 \text{ day}^{-1})$, $C_{cs} = C_{cs}(S, T, p)$ Oxie remineralisation $\hat{R}_{\text{omIox}} = k_{\text{oxI}} (1 - \varphi) [\text{POM}_1] ([\text{O}_2]/(C_{\text{hoxI}} + [\text{O}_2]))$ with $k_{\text{oxI}} = 0.32 \text{ yr}^{-1}$, $C_{\text{hoxI}} = 20 \mu\text{mol L}^{-1}$ remin. by nitrate reduction $\hat{R}_{\text{omInr}} = k_{\text{nrI}} (1 - \varphi) [\text{POM}_1] ([\text{NO}_3^-]/(C_{\text{hnrI}} + [\text{NO}_3^-])) (C_{\text{ioI}}/(C_{\text{ioI}} + [\text{O}_2]))$ with $k_{\text{nrI}} = 0.0032 \text{ yr}^{-1}$, $C_{\text{hnrI}} = 5 \mu\text{mol L}^{-1}$,